Accepted Manuscript

Interfacial friction in upward annular gas–liquid two-phase flow in pipes

Aliyu Musa Aliyu, Yahaya Danjuma Baba, Liyun Lao, Hoi Yeung, Kyung Chun Kim

Please cite this article as: A.M. Aliyu, Y.D. Baba, L. Lao, H. Yeung, K.C. Kim, Interfacial friction in upward annular gas–liquid two-phase flow in pipes, *Experimental Thermal and Fluid Science* (2017), doi: http://dx.doi.org/10.1016/j.expthermflusci.2017.02.006

1
2

Interfacial friction in upward annular gas–liquid two-phase flow in pipes

3   Aliyu Musa Aliyu[1], Yahaya Danjuma Baba[2], Liyun Lao[3], Hoi Yeung[3], Kyung Chun Kim[1*]

4   [1]School of Mechanical Engineering, Pusan National University, 609-735, Busan, Republic of Korea
5   [2]Department of Chemical and Petroleum Engineering, Afe Babalola University, PMB 5454, Nigeria
6   [3]Oil and Gas Engineering Centre, Cranfield University, Bedfordshire MK43 0AL, United Kingdom

7   **Abstract**

8   Accurate prediction of interfacial friction between the gas and liquid in annular two-phase flow in pipes is

9   essential for the proper modelling of pressure drop and heat transfer coefficient in pipeline systems. Many

10   empirical relationships have been obtained over the last half century. However, they are restricted to limited

11   superficial liquid and gas velocity ranges, essentially apply to atmospheric pressures, and the relationships are

12   only relevant for pipes with inner diameters between 10 and 50 mm. In this study, we carried out experiments in

13   a large diameter flow loop of 101.6 mm internal diameter with the superficial gas and liquid ranges of 11–29

14   m/s and 0.1–1.0 m/s respectively. An examination of published interfacial friction factor correlations was

15   carried out using a diverse database which was collected from the open literature for vertical annular flow. The

16   database includes measurements in pipes of 16–127 mm inner diameter for the liquid film thickness, interfacial

17   shear stress, and pressure gradient for air-water, air-water/glycerol, and argon-water flows. Eleven studies are

18   represented with experimental pressures of up to 6 bar. Significant discrepancies were found between many of

19   the published correlations and the large pipe data, primarily in the thick film region at low interfacial shear

20   stress. A correlation for the interfacial friction factor was hence derived using the extensive database. The

21   correlation includes dimensionless numbers for the effect of the diameter across pipe scales to be better

22   represented and better fit the wide range of experimental conditions, fluid properties, and operating pressures.

23   **Keywords:** Co-current annular flow, pressure gradient, interfacial shear stress, liquid film thickness,

24   vertical two-phase flow.

*Corresponding author
E-mail address: kckim@pusan.ac.kr (K.C. Kim)

25   **Nomenclature**

A. Roman

A	[m^2]	Cross-sectional area
D	[m]	Pipe internal diameter
e	[-]	Entrained liquid fraction
Fr	[-]	Froude number $= u/\sqrt{gD}$
f	[-]	Interfacial friction factor
g	[m/s^2]	Acceleration due to gravity
L	[m]	Pipe length
$\dot{m}$	[kg/s]	Phase mass flow rate
P	[Pa]	Local pressure
ΔP	[Pa]	Differential pressure
$-\dfrac{dP}{dz}$	[Pa/m]	Pressure gradient
Re	[-]	Reynolds number $= \rho u D/\mu$
t	[m]	Film thickness
u	[m/s]	Phase superficial velocity
x	[-]	Gas quality $= \rho_g u_{sg}/(\rho_g u_{sg} + \rho_l u_{sl})$
z	[m]	Axial distance along pipe

B. Greek

δ	Unit depends on quantity in question	Error in quantity indicated in bracket
ε	[-]	Void fraction
γ	[-]	Liquid droplet holdup
ν	m^2/s	Kinematic viscosity
μ	[kg/s-m]	Dynamic viscosity
ρ	[kg/m^3]	Density
σ	[N/m]	Surface tension
τ	[Pa]	Shear stress

C. Subscripts

c	Core
d	Droplet
e	Entrainment
g	Gas phase
i	Interfacial
l	Liquid phase
lf	Liquid film
s	Single phase
sg	Superficial gas
sl	Superficial liquid
w	Wall

26

2

1 Introduction

1.1 Background

Gas–liquid annular two-phase flow frequently occurs in many practical industrial applications. Common examples are gas condensates in oil and gas pipelines, evaporating and condensing flows in refrigeration systems and heat exchangers, and steam–water flows during nuclear reactor core cooling. This flow regime is characterised by the flow of liquid at the pipe inner wall periphery with a gas core flowing in the central region. At the interface between the two fluids, ripples and/or disturbance waves can be observed, the latter with high crests that can be sheared off at high gas velocities, which leads to liquid droplets being entrained in a highly turbulent gas core. These droplets can be re-deposited on the liquid film.

Because of the interactions of mass, momentum, and occasionally heat transfer at the interface, annular two-phase flows are complex and do not readily lend themselves to analytical modelling. Therefore, physically based models such as those based on two- or three-field models are usually solved numerically to obtain estimations of the phase fractions or pressure drop, which requires closure laws. Relations for closure laws include the fraction of liquid entrained as droplets and the interfacial friction factor, and they heavily rely on relevant experimental data.

The closure for interfacial friction factor deserves particular attention, because drag on the gas–liquid interface is dominant in the force balance (Belt et al. [1]). As will be shown later, the interfacial friction factor is an essential parameter in the force balance that couples the wavy film and the turbulent gas core. It is important to note that the interfacial friction factor differs from the two-phase friction factor. For the latter, a homogenous mixture is assumed to flow in the pipe and may be flow regime independent; therefore, mixture properties – density, viscosity and velocity – are hence defined and used. On the other hand, properties of the flowing gas are used in the case of the interfacial friction factor, where a momentum balance is done with the liquid film (not pipe wall) as boundary. Correlations for the interfacial friction factor derived by earlier investigators go back to Wallis [2] who used the analogy of single phase flow to propose a linear approximation to the

53 turbulent flow relationship in rough pipes. This works only for a small range of film thicknesses in the

54 low interfacial shear stress region. Since then, modifications based on his theory have been made (see

55 Belt et al. [1], [3]–[6]) but these correlations also fit limited ranges of data. Moreover, these do not

56 usually give good estimations when the inner pipe inner diameter goes beyond 100 mm (the observed

57 boundary between small and large diameter pipes).

58 Therefore many authors (Oliemans et al. [7]–Smith et al. [15]) insist that there is a need to

59 increase the knowledge of multiphase flow behaviour for large diameter pipe systems. For instance,

60 Oliemans et al. [7] compared entrainment correlations with large diameter test data and concluded

61 there is not much confidence in the predicted values of the correlations. Kataoka & Ishii [8] showed

62 that the use of the conventional drift flux model for pool void fraction prediction to relatively large

63 pipes was only limited to low gas fluxes, and thus had to develop a new correlation for large systems

64 where annular flow, for example, occurs at higher gas velocities. Disturbance waves which greatly

65 contribute to wall shear stress and are a source of entrained droplets were observed by Azzopardi et al.

66 [16] to be what they called "incoherent" in large diameter pipes. Careful observations revealed that in

67 large pipes, the waves were not perpendicular to the flow direction but were curved "bow waves" and

68 was also observed by Van der Meulen [17]. This contrasts to what obtains in smaller tubes where the

69 waves are continuous around the circumference (see Nedderman and Shearer [18], and Zhao et al.

70 [19]). The study by Omebere-Iyari and Azzopardi [20] on disturbance wave velocity provided strong

71 quantitative indication of pipe diameter effect on the gas–liquid interface behaviour. They established

72 that Pearce's coefficient, which is proportional the to wave velocity, increases with pipe diameter

73 until it reaches a constant value of 0.9 for large pipe diameters.

74 The foregoing means that the interaction between the fluids is different between the two pipe

75 scales and published data on large diameter pipes is scarce. It is therefore important to focus on

76 understanding the underlying mechanisms and finding more relationships that can apply to large pipes

77 for more optimal designs of pipeline systems.

78 **1.2   Previous interfacial friction factor correlations**

79 Table 1 summarises several previous correlations for the interfacial friction factor in upward gas–

80 liquid annular flow. It is pointed out that the interfacial friction factor is different from the two-phase

81 friction factor which is based on the wall shear stress rather than the interfacial shear stress. The latter

82 considers the flowing fluids as a homogenous mixture such that a mixture density and mixture

83 velocity are used to calculate the wall shear stress and hence frictional pressure drop. Therefore, the

84 prediction methodology is different from what is presented in this paper and correlations for the two-

85 phase friction factor (e.g. Klausner et al. [21], and Cioncolini et al. [22]) are not included in the table.

86 One of the earliest and most widely used correlations for the interfacial friction factor in two-phase

87 flow modelling is that by Wallis [2], which is essentially a linear fit of the friction factor against the

88 non-dimensional film thickness. Many modifications have been made to Wallis' correlation through

89 simple adjustments of the coefficients in order to fit experimental data (Belt et al. [1], Moeck [3], Fore

90 et al. [6], and Fukano and Furukawa [23]).

91

92 **Table 1: Reported interfacial friction factor correlations used for comparison with the current**
93 **experimental data**

94

95 Various correction methods were applied in order to update Wallis' correlation such as raising the

96 dimensionless film thickness to a power (Moeck [3]), introducing a function of the gas Reynolds

97 number (Fore et al. [6]), or introducing a ratio to account for the influence of a change in fluid

98 viscosity (Fukano and Furukawa [23]). As will be shown later, a plot of the Wallis-type correlations

99 against the present data and reported data shows that one curve cannot be used to represent all of these

100 data, as agreements that occur between some data and correlations do not occur with others.

101 **1.3   Experimental data from the open literature**

102   A total of 332 data points were collected for the vertical annular two-phase pressure drop in

103 smooth pipes. The data were obtained from 12 sources using pipes with internal diameters ranging

104 from 5 to 127 mm, including the current data. Key information about the sources in the database is

105 given in Table 2 with a breakdown of selected parameters provided in the histograms in Figure 1. All

106 the data are for macroscale gas–liquid flows obtained with transparent test sections, which allow for

107 visual identification of the flow regime. All data are in the annular flow regimes, so it is assumed that

108 there is little or no contamination from intermittent flow regimes such as slug or churn flows.

109

110 **Table 2: Experimental data for upward interfacial friction factor (all air/water except stated otherwise)**
111

112   Development lengths (L/D ratios) for the different datasets as reported by their authors were

113 examined and these are presented in Table 2. This is also shown in the histogram in Figure 1 (b), for

114 which most of the data were collected between 41 and 100 pipe diameters with the largest being that

115 of Owen [32] at 600 pipe diameters with 97 data points. Omebere-Iyari et al. [10] examined vertical

116 two-phase flow with different fluid combinations and concluded that L/D = 40 is sufficient for

117 reasonably well-developed flow after showing that the probability distribution functions (PDFs) of the

118 void fraction have very similar shapes at this value and higher. Their experiments were carried out at

119 46 bar pressure, and this may have facilitated the relatively short development length of 40 pipe

120 diameters. For the current study, the development length as given in Table 2 is 46 pipe diameters,

121 slightly higher than that of Omebere-Iyari et al. [10]. As will be shown later (in Section 3.2), we

122 observed that at L/D = 46 reasonably developed flow was produced. The inlet condition for the

123 upward section of the serpent pipe may have greatly assisted the relatively short development length.

124 This is because the momentum generated from the preceding downward flowing section is inherited

125 and this aids the upward flow development.

126

127   **Figure 1: Histograms showing selected parameters of the experimental database given in Table 2**

128

129   Four sets of data were obtained from experiments large diameter pipes. These sets include the current

130   study (101.6 mm) and those by Van der Meulen [17], Zangana [30], and Skopich [31] who

131   investigated flow in pipes with internal diameters of 127, 127, and 101.6 mm, respectively. The

132   remaining eight data sources are for smaller diameter pipes (less than 100 mm) ranging from 5 to 50.8

133   mm.

134   A majority of the measurements in the database are for air–water fluid combinations, except

135   for those of Alia et al. [34], and Fore and Dukler [35], who reported work on fluid combinations of

136   argon–water, and air/glycerine mixtures respectively. For system pressures, these runs range from just

137   below atmospheric pressure (0.9 bar) in the air and water study by Skopich et al. [31] to 6 bar by Alia

138   et al. [34] for argon and water. As shown in Figure 1 (c), the majority lie around atmospheric pressure.

139   Many data points (108) fall between 2 bar (Owen [32]) and 3 bar (Van der Meulen [17]).

140   The database contains experimental measurements on pressure gradients, and several of the

141   studies include direct measurements for liquid film thickness using conductance probes (the current

142   study, Belt et al. [1], Alia et al. [34], and Wongwises and Kongkiatwanitch [29]). Others determine

143   the liquid film thickness by measuring the cross-sectional void fraction and assuming a geometrically

144   uniform film along the pipe circumference [11], [17], [30], [31]. Owen [32] measured the entrained

145   droplet fraction in the gas core using the method of the isokinetic probe and estimated the droplet flow

146   rate. Others such as Fore et al. [6] measured the entrained fraction by sucking out the film using a

147   porous wall feature and subtracting from the liquid input. The entrained fraction is important in the

148   calculation of interfacial fraction factor from the measured pressure gradient, because the entrained

149   droplets change the properties of the gas core such as its density, and velocity. Belt et al [1] and Fore

150   and Dukler [36] noted that the entrained droplets can in some cases contribute up to 20% of the total

151   pressure gradient. Therefore, where entrainment occurs, this must be accounted for in the momentum

152   balance equation.

153   We performed experiments in a large diameter flow loop in order to collect data on interfacial

154   friction factor in upwards annular flow. Together with the diverse experimental database collected

155   from the open literature, we will show that earlier correlations for the interfacial friction factor from

156   small pipe measurements do not adequately represent data for large pipes and for conditions when the

157   liquid film is relatively thick. Consequently, a correlation will be proposed that better fits our data as

158   well as those from the diverse sources that cover a wider range of fluid velocities and pipe diameters.

2   Experimental setup and data processing

2.1   Description of flow loop

161   The experimental setup shown in Figure 2 is the Serpent Rig, an air/water facility at the Oil

162   and Gas Engineering Laboratory of Cranfield University. It is divided into three main parts: the Fluid

163   Supply (air and water) and Metering Area, the Test Area, and the Separation Section. The flow rig

164   receives measured flow rates of water and air from the Flow Metering area to the test rig and finally

165   into the ventilation tank, where the air and water are separated. The water is then returned to the

166   storage tank while the air is vented.

167   The Test Area consists of the flow loop, which is a pipeline that is approximately 20 m long

168   with an internal diameter of 101.6 mm (4 in.). The loop includes four vertical sections made from

169   ABS (acrylonitrile butadiene styrene) plastic with upward and downward flows and connected by

170   three Perspex 180-degree bends. The two 6-m vertical pipes in the middle are equipped with various

171   instruments that collect all the data. While the right arm of the U is the downward flowing section, the

172   left vertical section is the upward flowing section which is the area of interest of this study and where

173   all the data were collected.

174

175   **Figure 2: Serpent Rig facility indicating the upward section used for this study**

176   Flow metering equipment includes two air flow meters capable of measuring 0–4250 Sm^3/h

177   of air and a water flow meter with a range of 0.06–16 L/s. Six GE Sensing UNIK 5000 pressure

178 transducers (0–1.5 barg ±0.04%) are located at positions P2, P5, and P6 for the upward flow section.

179 Conductance probes are installed in the flow rig to measure the liquid film thickness, and a 32×32

180 grid capacitance wire mesh sensor (WMS) measures the cross-sectionally averaged gas void fraction,

181 which was used to identify the flow regime. Their locations are shown by dotted lines in Figure 2. A

182 DeltaV system and LabVIEW software were used for data acquisition. The DeltaV system records

183 and controls the air flow rates with a fixed sampling rate of 1 Hz, while LabVIEW acquires and

184 records the pressures, film thicknesses, and fluid temperatures using a sampling rate of 100 Hz.

185 Details about the design, calibration, and uncertainty analysis of the instrumentation are given in

186 previous studies [37]–[40].

187 **2.2   Instrumentation**

188 **2.2.1   Film thickness probes**

189   The conductance probe is one of the most common techniques for determining liquid holdup

190 in gas – liquid systems. It relies on measurements of electrical impedance between two electrodes in

191 contact with a conducting fluid and several configurations have been over the years depending on the

192 application and channel geometry. Its relative simplicity in application when compared to other

193 methods has been identified as a major advantage as well as the low cost of equipment involved.

194 Further details on types, principle of operation, design, and electronics can be found in the many

195 published articles are available in the open literature (e.g. Coney [41], Koskie et al. [42],

196 Tsocharitzidis et al. [43], and [44]). The film thickness probes used in this study were manufactured

197 in-house and the design is shown schematically in Figure 3.

198

199 **Figure 3: (a) film thickness sensor spool with four flush-mounted probes (b) details of individual sensor**

200 **design (all dimensions in mm) (c)) blocks of different diameters used for probe calibration (d) sample of**

201 **film thickness calibration curve (e) Repeatability tests for film thickness probes showing the mean film**

202 **thickness at u_{sl} = 0.1 m/s. For more conditions, see Almabrok** [37]

203

204   The spool consists of four film conductivity sensors which are evenly distributed

205   circumferentially to measure the circumferential distribution of the liquid film thickness at the

206   location where the spool is installed. As shown in Figure 3 (b) the sensing part of the conductivity

207   film thickness probe comprises a 10 mm diameter stainless steel rod and a stainless steel sleeve (18

208   mm outer diameter by 2 mm wall) arranged concentrically. Between them is a 2 mm thick insulation

209   layer. The end of the sensor is flush with the inner surface of the spool. Each conductor is electrically

210   in contact with the liquid film when the liquid film flows over them, so a conductive bridge is formed.

211   The conductivity and hence voltage between the two conductors is expected to change with the

212   thickness of the water film. The normalised output, i.e. ratio of output voltage to full scale voltage,

213   was used for calibration and measurements, as it minimises measurement errors caused by

214   inconsistent liquid conductivity and environmental factors such as temperature. The calibration was

215   carried out by using acrylic blocks (which like air, are electrical insulators) of known diameters

216   inserted into the probe spool concentrically to form a liquid layer with known thickness. Calibration

217   curves are plotted for the measured film thickness against normalised voltage output obtained offline.

218   Equations of these curves were used to convert online voltages obtained during experiments to film

219   thicknesses. Temperature correction coefficients for the sensors are regularly identified and applied

220   for correcting the temperature drift errors in the film thickness measurement. This is in done in

221   addition to the use of normalised film sensor outputs. The correction is applied to a temperature range

222   of 10–35 °C, which covers the two-phase mixture temperature range 15–22 °C in which the tests were

223   performed. During a test both the water and water/air mixture temperatures were logged so

224   temperature compensation was able to be implemented in order to obtain film thickness values during

225   the offline data processing. The repeatability of the liquid film thickness probes were checked by

226   performing triplicate runs at a constant superficial liquid velocity and the full range of superficial gas

227   velocities between 12.5 and 28.9 m/s. Figure 3 shows a plot of such a test at 0.1 m/s. A standard

228   deviation of 0.1 mm in repeated film thickness measurements was established as a result, and this

229   gives a ±3.3% full scale error in the film thickness measurement. It is also possible that inlet/outlet

230   stability could also add to small changes in the repeatability of the test, and this may have also

231   contributed in the ±3.3% difference between respective measurements. It was considered that the

232   uncertainty caused by calibration to be much smaller in comparison, and hence negligible, since the

233   calibration curves of the probes give R-square values of 0.99 and above for fifth-degree polynomials.

234   **2.2.2   Wire mesh sensor (WMS)**

235   The capacitance Wire Mesh Sensor (WMS) used for the cross-sectional void distribution

236   measurement at the stated locations along the pipe axis has a 32×32 wire grid (Figure 2 (c)). The

237   sensor, associated electronics and data processing software were provided by Helmholtz–Zentrum

238   Dresden–Rossendorf, Germany. The method of phase fraction distribution measurement in air/water

239   flows using similar WMS has been validated by a number of studies (Prasser et al. [45] and Da Silva

240   et al. [46]). In the sensor assembly, wire electrodes perpendicular to each other are across the flow

241   cross-sectional area.

242

243

Figure 4: Capacitance wire mesh sensor used in this study

244   One set of the perpendicular wires acts as signal sender, while the other acts as receiver. The

245   WMS measures the local permittivity of the fluid in the gaps of each crossing point by continuously

246   applying an excitation voltage (of 5 MHz) to each sender electrode while keeping others at ground

247   potential then synchronously measuring the alternating current flow to all receivers. Based on these

248   measurements, the cross-sectional fluid distribution across the pipe the sensor can be estimated. For

249   the sensor used in this study, the separation between the sender and receiver planes of wires is 2.5 mm.

250   The spacing between two wires in parallel is 3.2 mm. A sampling rate of 1000 frames per second is

251   used for the measurement. Validation studies were carried out on the measurement accuracy of the

252   present WMS system and it was reported by Almabrok et al. [39] that errors of around ±10% are

253   obtainable. Further reading on the theory and principles of operation of the WMS can be found in the

254   works of Prasser et al. [45], Da Silva et al. [47], and Da Silva et al. [48].

255   **2.3   Data processing**

256   **2.3.1   Film velocity and entrained droplet fraction**

257   The entrained droplet fraction was calculated from measurements obtained for the liquid film

258   thickness discussed earlier, and the liquid film velocity measurements. Mean liquid film velocity

259   measurements were made using the electrolyte injection method. The method involves injecting

260   sodium chloride electrolyte into the liquid film to create a surge in conductivity. The transit time of a

261   conductivity surge between two identical sensors 100 mm apart in a probe spool is determined using a

262   cross-correlation algorithm in MATLAB. The film velocity is then calculated by dividing the distance

263   by the signal transit time or time delay between the two sensors. The assumption here is that as the

264   liquid films are very thin ($\sim 1 - 1.5\ mm$), the velocity profile within the film is such that the wave

265   (or structure) velocities are close to the bulk film velocity, meaning velocities with higher uncertainty

266   for the thicker films. Nevertheless, uncertainties of around ±8% in the film velocity measurements

267   were produced and this has been discussed extensively [40].

268   Using the definitions given in

269   Figure 5, the measured velocities can then be used to calculate the entrained droplet fraction

270   using the relationship:

$$e = \frac{\dot{m}_l - \dot{m}_{lf}}{\dot{m}_l} = \frac{\rho_l u_{sl} A - \rho_l u_{lf} A_{lf}}{\rho_l u_{sl} A} = 1 - \frac{4 u_{lf} t}{u_{sl} D} \tag{1}$$

271   where $\dot{m}_l$, and $\dot{m}_{lf}$ are the total liquid flow rate and liquid film flow rate in kg/s, while e, t, u_{lf}, u_{sl},

272   and D are the entrained liquid fraction, measured film thickness, measured film velocity, liquid

273   superficial velocity and pipe internal diameter respectively. Tabulated and graphical results obtained

274   using Equation (1) for different flow conditions are given in Almabrok [37] and Aliyu et al. [40].

275

276   **Figure 5: Representation of annular flow with droplets**

277   Figure 6 (a) and (b) show typical examples of time series data collected for the liquid film

278   thickness and pressure gradient. The measurement conditions include a superficial liquid velocity of

279   1.0 m/s and superficial gas velocity of 18.56 m/s. Data were recorded for 2 minutes per run, but the

280   figures show the behaviour for 10 seconds only. The wavy nature of the liquid film recorded by the

281   conductance probe is clearly seen in Figure 6 (a) with wave heights that are one to two times greater

282   than the thickness of the base film. This behaviour has widely been reported for annular films (Hall

283   Taylor et al. [49], and Sawant et al. [50]).

284   **Figure 6: Examples of time series data for (a) liquid film thickness and (b) pressure gradient with a**
285   **superficial liquid velocity of 1.0 m/s and superficial gas velocity of 18.56 m/s**

286   For subsequent steady-state analyses, the time series data were averaged over the whole two-

287   minute recording time, as shown in Table 3. For all superficial liquid velocities, the liquid film

288   thickness increases with superficial liquid velocity but decreases with increasing gas velocity. This

289   decrease with gas velocity is asymptotic for vertical upflow regardless of liquid velocity and viscosity

290   (see Fukano and Furukawa [23]). Equation (2) is the steady-state momentum balance for the two-

291   phase mixture flowing upwards in the pipe:

$$-\frac{dP}{dz} = \{\rho_c \varepsilon + \rho_l (1 - \varepsilon)\} g + \frac{4}{D} \tau \tag{2}$$

292   Where ρ_g and ρ_l are the gas and liquid densities respectively; ε is the time-averaged cross-sectional

293   void fraction. The first term on the right hand side of the equation refers to the gravitational

294   component of the pressure gradient; the second is the frictional component with τ being the shear

295   stress, which consists of the wall and interfacial shear stresses:

$$\tau = \frac{1}{2}\{f_w \rho_l (1 - \varepsilon) u_{lf}^2 + f_i \rho_c \varepsilon (u_c - u_{lf}) |u_c - u_{lf}|\} \tag{3}$$

13

296   where f_w and f_i are the wall and interfacial friction factors respectively. As shown in Table 3, for all

297   superficial liquid velocities, the liquid pressure gradient increases with the gas superficial velocity.

298   This is easily explained by Equations (2) and (3), where the frictional component of the pressure

299   gradient increases as the superficial fluid velocities increase. Wall friction increases as liquid velocity

300   increases; while interfacial friction increases with increasing slip at the gas–liquid interface, and this

301   is more affected by the core velocity since the liquid velocity does not change by as much.

302

303   **Table 3: Averaged measured quantities for the air–water system in the upward section of the Serpent Rig**

304

305   A flow regime map for upward flow was produced using visual observations and this is

306   presented in Figure 7 (a). Flow regimes that are either bubbly or churn are marked as "other" and

307   these have been excluded from the data in Table 3. The regimes were identified with the help of

308   videos made from WMS reconstructed images. Specially designed software was used to stack the

309   images acquired at 1000 fps and these can be played back at slower speeds than real-time. Example

310   snapshots of the videos at $u_{sl} = 0.2$ m/s are shown in Figure 7 (a) and they were used to differentiate

311   flow at $u_{sl} = 9.7$, and 12.09 m/s. It can be seen that for the former condition, the gas core is not

312   continuous. Large liquid lumps can be seen to be torn off from base film. Such a flow was not

313   classified as annular since some up and down oscillatory movement was observed. The regime was

314   ultimately classified as "churn" flow and screened out from those used for the subsequent analyses in

315   this paper. At critical conditions near flow regime transition regions, identification is difficult to

316   achieve with the naked eye, and this underscores the importance of using the WMS. Conversely, the

317   snapshot on the top right-hand corner of Figure 7 (a) was classified as annular where a distinct gas–

318   liquid interface and a continuous gas phase can be seen.

319   Figure 7 (b) is a plot of measured pressure gradient (dP/dz) for the upward flow section. For

320   all superficial liquid velocities, dP/dz values decrease with increasing gas velocity. There is a decrease

321 in dP/dz because increasing gas void fraction results in decreasing cross-sectional liquid holdup and

322 the liquid contribution to the gravitational pressure gradient also decreases. However, a minimum is

323 reached when increasing the gas velocity results in the frictional component of dP/dz equalling the

324 gravitational component. This results in a competition between inertia and gravity forces and

325 oscillatory behaviour is observed with the liquid. The minimum dP/dz is a critical point corresponding

326 to a flow regime transition from churn to annular flow (see Hewitt and Hall-Taylor [51], McQuillan

327 and Whalley [52], and Hewitt [53]). Further increasing the gas velocity causes the pressure gradient to

328 increase due to the increasing dominance of the frictional component over the gravitational

329 component. The flow is now in the annular region and the conditions for this study were chosen from

330 this region indicated by the closed markers in Figure 7 (b).This is agrees with our visual observations

331 as well as the reconstructed WMS images.

332

333 **Figure 7: Effect of fluid superficial velocities on flow regime map produced by visual observations aided**
334 **by WMS visualisation**

335

336 **2.3.2   Determination of interfacial friction factor from measurements**

337 From the foregoing discussion, the pressure gradient, liquid film thickness and velocity measurements

338 obtained for this study were verified to be in the annular region. These were used to calculate the

339 interfacial friction factor, which in fully developed annular two-phase flow is defined as:

$$f_i = \frac{2\tau_i}{\rho_g u_{sg}^2} \tag{4}$$

340 The superficial gas velocity u_{sg} in this work is calculated based on the whole pipe cross-sectional

341 area. In many cases, droplets are torn off from the crests of the liquid film (or atomised) and become

342 entrained in the gas core, thereby affecting its density. The interfacial friction factor thus becomes:

$$f_i = \frac{2\tau_i}{\rho_c u_c^2} \tag{5}$$

15

343   where the subscript c denotes the core region. The following three steps are used to determine the core

344   velocity, core density, and the interfacial friction factor respectively:

345   *1. Core velocity*

346   Estimation of the core density ρ_c requires knowledge of the liquid film velocity, which was

347   determined experimentally for the present dataset. Details are well documented for the measurement

348   technique using cross correlation of conductance signals from adjacent axial probes and the

349   corresponding uncertainties [37], [38], [40], [54]. The core velocity u_c is estimated by writing a mass

350   balance of the gas input, which yields the relationship for the mean velocity for the gas core (see

351   Vieira et al. [55]):

$$u_c = \frac{(u_{sg} + u_{sl}e)D^2}{(D - 2t)^2} \tag{6}$$

352   where t is the measured mean liquid film thickness assuming it is circumferentially uniform, and e is

353   the entrained droplet fraction determined experimentally. In cases where experimental data for e was

354   not available, it was calculated using the correlation of Cioncolini and Thome [56]. Other empirical

355   correlations exist such as those of Ishii and Mishima [57], and Sawant et al. [58].

356

357   **Figure 8: Representation and notation of the various phases (film, gas, and droplets) occupying the total**

358   **pipe area. Subscript d denotes droplets. Where γ, ε, and ε_c are the droplet holdup, void fraction and core**

359   **void fraction respectively (Cioncolini et al. [22])**

360   *2. Core density*

361   The density ρ_c of a gas core laden with entrained droplets used in Equation (5) is calculated

362   as the arithmetic mean of the pure gas and liquid droplet densities:

$$\rho_c = (1 - \varepsilon_c)\rho_l + \varepsilon_c\rho_g \tag{7}$$

363   where ε_c (Figure 8) is the gas core void fraction estimated as:

$$\varepsilon_c = \frac{\varepsilon}{\varepsilon + \gamma(1 - \varepsilon)} \tag{8}$$

364   ε is the cross-sectionally averaged void fraction, and γ is the droplet holdup. An expression for the

365   droplet holdup γ can be obtained using the definition of the entrained droplet fraction e which is the

366   ratio of the entrained liquid droplet mass flow rate $\dot{m}_d$ to that of the total liquid mass flow rate $\dot{m}_l$ i.e.:

$$e = \frac{\dot{m}_d}{\dot{m}_l} = \frac{\rho_l u_d A_d}{\rho_l u_{sl} A} = \frac{u_d A_d}{u_{sl} A} \tag{9}$$

367   If the phase slip between the droplets and the carrier gas is ignored, the droplets travel at the velocity

368   of the carrier gas, therefore $u_d = u_g$. Equation (9) now becomes:

$$e = \frac{u_g A_d}{u_{sl} A} = \frac{\frac{u_{sg}}{\varepsilon} A_d}{u_{sl} A} \tag{10}$$

369   Substituting the relation for the cross-sectional area occupied by the droplets A_d based on the phase

370   splits as shown in Figure 8, we can rewrite Equation (10) as follows:

$$e = \frac{u_{sg}}{u_{sl}} \frac{\gamma(1 - \varepsilon)}{\varepsilon} \tag{11}$$

371   The gas quality x is defined as the ratio of the gas mass flux to the total gas mass flux; i.e. $x =$

372     $\rho_g u_{sg} / (\rho_g u_{sg} + \rho_l u_{sl})$. Rearranging it as $\frac{u_{sg}}{u_{sl}} = \frac{x \rho_l}{(1-x)\rho_g}$ and substituting in Equation (11) yields:

$$e = \frac{x \rho_l}{(1 - x)\rho_g} \frac{\gamma(1 - \varepsilon)}{\varepsilon} \tag{12}$$

373   which can be rearranged to the following to give an expression for the droplet holdup for use in

374   Equation (8):

$$\gamma = e \frac{\varepsilon}{1 - \varepsilon} \frac{1 - x}{x} \frac{\rho_g}{\rho_l} \tag{13}$$

375   ### *3. Interfacial shear stress*

376   The interfacial shear stress τ_i is obtained from a momentum balance around the gas core in the axial

377   direction of the flow, as shown in Figure 9. It is assumed that the flow is fully developed, at steady

378   state, and at equilibrium where the rate of droplet entrainment equals the rate of droplet deposition.

379   Therefore,

$$\tau_i = \frac{D - 2t}{4}\left(-\frac{dP}{dz} - \rho_c g\right) \tag{14}$$

where $-dP/dz$ is the measured pressure gradient. For a detailed derivation of Equation (14), see Fore et al. [6], and Wongwises and Kongkiatwanitch [29]. Equations (6)–(14) can then be used to calculate the interfacial friction factor as defined in Equation (5).

Figure 9: Control volume for the momentum balance in Equation (14). Based on the schematic by Wongwises and Kongkiatwanitch [29]

3 Discussion of results

3.1 Flow regime maps

The conditions for the current experiments and those obtained from the literature were plotted together on the Taitel et al [59] flow regime map, as shown in Figure 10. It can be seen that all the data points chosen for this study fall in the annular flow region. Taitel et al's [59] flow regime map was constructed using physically based mechanisms which underlie each transition. They also derived models for the transitions based on these mechanisms. Along with the Hewitt and Roberts [60] flow regime map (Figure 11Figure 11), it is one of the most widely used for gas–liquid flow in vertical pipes. The test conditions range from the near annular transition (e.g. Van der Meulen [17], and Alia et al. [34]) to the fully annular flow region (e.g. Shearer and Nedderman [61]). Flow regime transitions are not sharp and occur within a range of superficial fluid velocities, which could be affected by the liquid viscosities and densities of liquid and gas phases. As a result, data points that may seem to fall in the churn flow region of the map were actually observed to be annular flow. For example, Alia et al. [34] report data that are deeply within the annular flow regime region when plotted on the Hewitt and Roberts [60] flow regime map shown in Figure 11Figure 11, but these points fall in the annular flow region nearer the transition areas when plotted on the Taitel et al. [59] flow regime map. However, in the flow regime map published by Shell [62] and shown in Figure 12, the conditions for the entire database can be seen to be in the annular flow region. The flow regime

405   map is based on the gas and liquid Froude numbers on the horizontal and vertical axes respectively.

406   Here, the Froude numbers are densimetric and defined as follows:

$$Fr_g = u_{sg}\sqrt{\frac{\rho_g}{(\rho_l-\rho_g)gD}} \, , Fr_l = u_{sl}\sqrt{\frac{\rho_l}{(\rho_l-\rho_g)gD}} \tag{15}$$

407

408

409   **Figure 10: Experimental data against the Taitel et al.** [59] **flow regime map at (a) 1 bar (b) 2.5 bar**
410   **pressure**

411

412   **Figure 11: Experimental data bank against Hewitt and Roberts** [60] **flow regime map showing all data**
413   **are in the annular flow regime**

414

415

416   **Figure 12: Experimental databank against the Shell** [62] **flow regime mapFilm thickness, void fraction,**
417   **and flow development**

418   The measurement station within the dotted circle of the upward flowing section of the flow

419   rig in Figure 2 is located at 46 pipe diameters from the bottom bend. An extensive study on axial

420   variation of measured quantities along the straight sections of the rig was reported in the doctoral

421   thesis of Almabrok [37]. It showed that a significant reduction in entrance effects is already achieved

422   on reaching the top location. Time series and probability distribution functions of film thickness,

423   pressures, and void fraction exhibited similar established flow at the top (L/D = 46 from the U-bend)

424   and middle positions (L/D = 28). These tendencies substantially differ from those observed at the

425   bottom position (L/D = 5) which exhibited flow maldistributions due to bend effects. Confirmation of

426   flow development was done by observing slow-motion videos made by stacking individual WMS

427   frames (achieved using specially designed software).

428

429   **Figure 13: Normalised liquid film thickness axial development in the upwards flowing section of the rig**
430   **(See Almabrok [37] for more)**

431

432   Figure 13 shows normalised mean film thicknesses obtained from the conductance probes at
433   the stated axial positions for u_{sl} **= 0.2, 0.3,** and 0.48 m/s. The normalised film thickness here is
434   defined as the ratio of film thickness at other L/D positions to that at L/D = 46 (i.e. t_{norm} **=**
435    $t/t_{L/D=46}$). This means that t_{norm} at 46 pipe diameters is unity. The error bars shown in the graphs
436   were calculated as errors propagated from the ±3.3% uncertainty in the film thickness probes; and
437   these are $\sqrt{\mathbf{3.3^2 + 3.3^2}}$ **= ±4.7%**. It can be seen that there is minimal change in the normalised mean
438   film thickness between the middle and bottom positions. Similarly, Figure 14Figure 14 shows the
439   normalised void fraction obtained from the WMS at L/D = 5, 28, and 46 positions from the bottom U-
440   bend for u_{sl} **= 0.2, 0.48,** and 1.0 m/s. The void fractions were normalised with respect to that at L/D
441   = 46 such that ε_{norm} **=** $\varepsilon/\varepsilon_{L/D=46}$ and ε_{norm} **= 1** at L/D = 46. The error bars shown in the graphs for
442   ε_{norm} were calculated as errors propagated from the ±10.0% uncertainty in the WMS; and these are
443    $\sqrt{\mathbf{10.0^2 + 10.0^2}}$ **= ±14.4%**. Again, as shown, the ratios at the bottom position reach up to 1.2 in
444   contrast to those obtained at the middle which converges very close to 1. The effect of superficial
445   liquid velocity can be seen from Figure 13 and Figure 14. As liquid velocity increases, there is
446   increasing disparity between the film thickness/void fraction ratios at the bottom positions of the pipe
447   for different gas velocities. However, the ratios become similar by converging towards unity for all
448   conditions once the flow reaches the middle part of the pipe. While L/D = 46 is one of the least in the
449   database collected (see Table 2), flow development is helped by the momentum gathered in the
450   downward flowing section and transferred as the flow negotiates the bend to the upward flowing
451   section. Therefore, the data used for the analyses in this paper are those at L/D = 46, represent highly
452   developed upwards annular flow (fully developed flow is difficult to achieve and requires very long
453   pipes). Additional details can be found in Almabrok [37].

454

455   **Figure 14: Normalised gas void fraction axial development in the upwards flowing section of the rig**

456

457   **3.2   Comparison of experimental friction factors and existing correlations**

458   The interfacial friction has an inverse relationship with the gas Reynolds number as expected,

459   which is akin to the turbulent flow region of the Moody Chart for single-phase flow. The gas

460   Reynolds number used is here is based on the superficial gas velocity and pipe diameter i.e.

$$Re_g = \frac{\rho_g u_{sg} D}{\mu_g} \tag{16}$$

461   Fore et al. [6] note that the at sufficiently high Reynolds numbers, the interfacial friction

462   factor reaches an asymptotic value and at such conditions, the friction factor becomes dependent only

463   on the relative liquid film thickness. Nevertheless, it is clear that the gas Reynolds number is a

464   candidate for interfacial friction factor correlation, and one curve that is a function of the Reynolds

465   number only cannot represent all the data. Other parameters representing the different experimental

466   conditions, pipe scales, and fluid properties need to be considered. This is perhaps evident from the

467   different trends exhibited by the various datasets, because the ranges of liquid flow rates and pipe

468   sizes widely differ. Error analysis of the interfacial friction factor is given in the Appendix, and this

469   shows relative errors of ±6–14%.

470   A plot of f_i vs t/D values for the current experiments, as well as those from previous studies

471   is given in

472   Figure 15. It can be seen that there are general under- and over-predictions that are magnified

473   as t/D increases. For instance, the measurements by Shearer and Nedderman [33] and those by Owen

474   [32] are within 50% of the values predicted by the correlations of Wallis [2], Moeck [3], and Fore et

475   al. [6] at low t/D values, but they deviate by more than 10 times at higher values. One reason for the

476   general agreement at small t/D values could be that most data and correlations were obtained at

477   conditions in the full annular region, where the films are thinner and smoother. These are far from the

478 transition region where thick and rough films are found. With the dimensionless film thickness being

479 able to show the behaviour of the interfacial friction factor within the various regions of annular flow,

480 it is therefore a relevant parameter in correlating interfacial friction factor data.

481

482

483 **Figure 15: Experimental interfacial friction factors versus superficial gas Reynolds number**

484
485

486 **Figure 16: Comparison of current and other experimental friction factors with Wallis-type correlations**

487 Another group of f_i correlations have Wallis-type structure but no functional dependence on

488 t/D. Examples are those by Ambrosini et al. [26], and Holt et al. [28] who use several combinations

489 of the bulk gas Reynolds and Weber numbers. Asali et al. [5] and Ambrosini et al. [26] used

490 correlations with the film thickness (t^+) non-dimensionlised by the friction velocity. Implementation

491 of these equations is iterative since they are implicit functions of the interfacial friction factor. As

492 shown in Figure 17 (e) and (h), these correlations provide good predictions in the higher shear regions,

493 where the films are thinner and smoother but rapidly deteriorate for thicker films. Asali et al. [5] and

494 Ambrosini et al. [26] used similar databases for their correlations, which included data obtained from

495 pipes with internal diameter of 10–42 mm and fluid combinations of helium and

496 hydrocarbons/glycerine mixtures, in contrast to the air or steam/water combinations mostly

497 considered in the present database.

498 Hori et al. [24] opted for a direct power law relationship for the friction factor using the

499 Reynolds and Froude numbers of the gas and liquid. The Froude numbers are defined as follows:

$$Fr_g = \frac{u_{sg}}{\sqrt{gD}} , Fr_l = \frac{u_{sl}}{\sqrt{gD}} \tag{17}$$

500 Their correlation produced good estimations at low values of the interfacial friction factor. However,

501 as shown in Figure 17 (d), substantial over-estimations occur at high values of f_i corresponding to low

502 gas flow regions where the liquid films are thick and rough. Again, this is because the experimental

503 conditions do not cover these regions. Wongwises and Kongkiatwanitch [29] also used a power law

504 relationship for their friction factors obtained in a 29-mm pipe at atmospheric pressure. They used the

505 gas Reynolds number and the non-dimensional film thickness t/D as their correlating dimensionless

506 numbers and their correlation was less successful over the experimental database.

507   In summary, these interfacial friction factor correlations were developed with data obtained

508 for small pressure ranges. For example, Fukano and Furukawa [23] carried out measurements at

509 around 1 bar, Holt et al. [28] used 0.2–1.5 bar, Ambrosini et al. [26] used 0.2–1.9 bar, and Asali et al.

510 [5] used 1–2 bar. Only Fore et al. [6] had a wider range of test pressures than the current database at

511 3.4–17 bar for experiments with air–water, air–water/glycerine, and nitrogen–water gas–liquid

512 combinations. However, their experiments were conducted with a small diameter pipe and in the thin

513 film region, in contrast to the current database of larger and smaller-diameter pipes containing much

514 thicker liquid films.

515   It is clear that there is a need to extend the applicable range of prediction methods for the

516 interfacial friction factor. While a mechanistic or physical approach is desirable, it has not been

517 achieved due to the difficulties introduced in annular two-phase flow by high turbulence and complex

518 momentum transfer across the highly deformable gas–liquid interface. Improvements may be

519 achieved using correlations over broader ranges of flow conditions and tube sizes. We therefore

520 propose a new correlation using a more diverse database.

521

522

523 **Figure 17: Comparison of 332 interfacial friction factor data points with predictions of various**
524 **correlations**

23

525   **3.3   Correlation of interfacial friction factor**

526   Fore et al. [6] noted that the Wallis correlation and other correlations with Wallis-type dependency on

527   t/D do not adequately account for changes in Reynolds number in annular flow. They are best

528   applied in annular flow where the dependence on the Reynolds number is minimal, such as for thin,

529   smooth films. In such a situation, the friction factor depends on only the dimensionless film thickness

530   and has been argued to have linear dependence (e.g. Belt et al [1]). However, this conclusion is based

531   on only a small number of data points collected in a small-diameter pipe in the annular flow regime.

532   For films that are deeply in the annular regime and especially in large pipes, the flow behaviour

533   cannot be dictated by the rough film mechanism because these films are smooth and thin.

534   Azzopardi [37] and Jayanti et al. [64] show that the waves on the crests of the film in large

535   pipes are circumferentially incoherent, meaning that they cover only a part of the tube circumference.

536   They therefore do not solely dictate the flow behaviour, and the flowing gas plays a vital role in

537   determining many of the flow characteristics, including interfacial friction. It is thus necessary to fit

538   the friction factor data in order to reflect other parameters that dictate the flow behaviour, not only the

539   dimensionless film thickness as in the classic correlations. The following form is therefore proposed

540   for the interfacial friction factor:

$$f_i = f_s \left[\mathbf{1} + a(t/D)^b Re_g^j Fr_g^k \right]^l \tag{18}$$

541   Where $f_s = \mathbf{0.046} Re_g^{0.2}$. Equation (18) includes the gas Reynolds and Froude numbers (defined in

542   Equation 17) but essentially retains the form of a Wallis-type correlation. This preserves the

543   behaviour of the Wallis correlation, which works quite well at small values of t/D (Figure 16 and

544   Figure 17). The Reynolds number ensures that the correlation captures inertia changes in the gas core.

545   The gas Froude number is included because it is a ratio of inertial forces of pressure-driven gas/liquid

546   flow to the opposing gravitational force, particularly important for high-velocity gas flows in vertical

547   upward annular two-phase flow. The inertial forces dominate gravitation, resulting in $Fr_g > \mathbf{1}$ and this

548 is termed supercritical flow where the tendency of films to flow downwards is overcome by inertia

549 from the gas flow. $Fr_g \approx \mathbf{1}$ is the critical gas Froude number at the flow reversal point. In fact, authors

550 such as Wallis ([2], [65]) and Barbosa et al. [66] have used $Fr_g > \mathbf{1}$ as a criterion for the transition

551 from churn to annular flow and annular flow. If $Fr_g < \mathbf{1}$, annular flow is not considered to have

552 occurred and the flow is still in the churn regime where film oscillations occur due to the two

553 competing forces. Therefore, the inclusion of the gas Froude number is consistent with the

554 phenomenon of annular flow. Partial correlational analysis with other dimensionless numbers such as

555 the core Reynolds, and Weber numbers as well as the liquid Reynolds number showed that these have

556 little effect on the interfacial friction factor.

557 　　　Non-linear least squares regression with the entire experimental database yields the following

558 correlation:

$$f_i = f_s \left[\mathbf{1} + \mathbf{0.3}(t/D)^{0.12} Re_g^{0.54} Fr_g^{-1.20} \right]^{1.5} \qquad (19)$$

559 where Re_g and Fr_g are defined in Equations (16) and (17). The correlation is valid for $D^* > \mathbf{2}$, where

560 $D^* = D/\sqrt{\sigma/g(\rho_l - \rho_g)}$ the dimensionless hydraulic diameter as defined by Kataoka and Ishii [8].

561 Pipes with D^* greater than about 37, corresponding to $D = 100$ mm, are considered to be large

562 diameter. For $D^* < \mathbf{2}$ corresponding to $D < \mathbf{5}$ mm, Equation (19) may not apply due to lack of

563 representative data (for $D < \mathbf{5}$ mm) in the databank. For such pipes capillary forces will be prevalent

564 and non-dimensional quantities such as the Capillary number (Ca) may be used to correlate data.

565 Figure 18 shows that this correlation fits the data better than any of those in Figure 17 (a)–(m). From

566 the figure, it is evident that there is a clear segregation in the magnitudes of the experimental friction

567 factors along pipe scales, with the larger pipes having higher interfacial friction factors. This might

568 seem surprising at first but is entirely logical since larger pipes produce smaller relative slip between

569 the phases compared to small-diameter pipes (i.e., a lesser value of $(u_c - u_{lf})$).

570

571   **Figure 18: Predictions of proposed correlation compared with entire experimental database**

572

573   For the gas Reynolds number in the proposed correlation, the positive index of 0.55 may seem

574   inappropriate at first, given that there is always an inverse relationship between friction factors and

575   the Reynolds number or fluid velocity. This is also true in the present case, as the superficial gas

576   velocity inherent in Re_g and Fr_g carries a net negative index of –0.66, which is within the range of –

577   0.6 to –0.89 obtained for the index of Re_g by previous authors in their correlations for f_i (Fore et al.

578   [6], Wongwises and Kongkitatwanitch [29], Hori et al. [24], Ambrosini et al. [26], and Holt et al.

579   [28]). Furthermore, t/D in Equation (19) is raised to a power of 0.1 which is a rather small number

580   indicating a lesser than expected dependence of f_i on film thickness. This was explained by

581   Cioncolini and Thome [67] and Narcy [68] to be because the velocity profile in the film is

582   concentrated in the region near the pipe wall. This near wall region is much smaller than the film

583   thickness, hence the small power on t/D.

584   The computed statistics (MSE, MAE, etc.) show that the proposed correlation predicts the

585   current database quite well. It exhibits the lowest values of mean square error (MSE) (see Table 4).

586   Although other correlations have comparable values (e.g. those of Asali et al. [5], and Hori et al. [24]),

587   their predictions have much higher mean absolute error and lower number of points within the ±50%

588   error band. Over half of the predicted points lie within the ±50% error band for the correlations

589   reported by Asali et al. [5], Fore et al. [6], and Wongiwises and Kongkiatwanitch [29], as shown in

590   the table. However, these values carry a bias based on the large number of data from small pipes, and

591   the data are mostly for relatively thin films, as shown in

592

593   Figure 16 and Figure 17. As stated earlier, the shape, size, and localisation of the waves in

594   large pipes have been shown by many authors in the past to differ from smaller pipes and these

595   features affect the manner in which droplet entrainment/deposition and momentum transfer occur. The

596   new correlation can be used as a closure relationship in numerical codes to produce better predictions

597   of interfacial friction factor, especially in the thick film regions where the gas velocity is low (around

598   15–20 m/s) and the gas–liquid interface is rougher.

599

600   **Table 4: Statistical comparison between predictions of proposed and previous correlations**

601

602   While no correlations are universally acceptable, due to their limited or lack of physical insight,

603   we suggest a more mechanistic approach for future work. This is not easy since the turbulent gas–

604   liquid interface presents unique challenges of momentum transfer by droplet deposition and

605   entrainment. There are currently no mechanistic models for droplet entrainment and deposition, which

606   adds another layer of difficulty for such a methodology. Another approach towards improvement

607   could be correlations fitted with more local measurements of local phenomena rather than with bulk

608   properties of the film and flowing gas. However, this will require the collation of a large pool of more

609   local measurements such as the disturbance wave heights, wave frequencies for the film, and velocity

610   profiles within both phases. Complete sets are currently scarce or remain largely unpublished. The

611   addition of evaporating, boiling, condensing flows, and data from experiments conducted in

612   microgravity will also expand the applicable ranges of new empirical models. Nevertheless, as shown,

613   the current correlations can be used with more confidence, given that they have been developed from

614   a broader range of flow conditions and pipe diameters than what has been reported.

615   **4   Conclusions**

616   In this study experiments were performed using a large diameter flow loop of 101.6 mm internal

617   diameter within the superficial gas and liquid ranges of 11–29 m/s and 0.1–1.0 m/s respectively. Data

618   on pressure gradient, as well as film thickness were collected in the annular flow regime and these

619   were used to calculate the interfacial friction factor. The effectiveness of using existing prediction

620   methods for the interfacial friction factor was then examined in large-pipe annular flow, as well as in

621   small-pipe flow from a variety of sources. These sources include data from a wide spectrum of flow

622   conditions and pipe sizes. For example, the range of pipe diameters is 20–127 mm, and the data are

623   obtained from experiments performed with air–water, argon–water, and air–glycerol combinations as

624   the test fluids. The interfacial friction factor is one of the important parameters in determining

625   pressure gradient in the annular flow regime. However, our analyses show that many of the previous

626   correlations can be inadequate when used outside certain ranges of experimental conditions,

627   especially for large industrial pipe simulations. Nevertheless, many of these are used as closure laws

628   in commercial thermal-hydraulic codes based on one-dimensional two- or three-fluid models. The

629   results indicate the following:

630   • Previous correlations for the interfacial friction factor of vertical annular flow are mostly

631   arithmetic modifications of Wallis correlation ($f_i = 0.005[1 + 300t/D]$), where the intercept

632   and/or factor are changed to fit ranges of experimental conditions.

633   • Wallis-type correlations which are functions of only t/D give some deviations of f_i

634   predictions for thicker liquid films especially in large diameter pipes.

635   • The proposed correlation ($f_i = f_s[1 + 0.3(t/D)^{0.12}Re_g^{0.54}Fr^{-1.20}]^{1.5}$) gives better

636   description of the interfacial friction factor in upward annular flow across pipe scales in the

637   database. It maintains the shape and characteristics of the Wallis-type dependency on the

638   dimensionless film thickness at low t/D values. However, introducing simple functions of the

639   core Reynolds and Froude numbers ensures its relevance for thicker films.

640   As mentioned, mechanistic methodologies are required to provide more generally applicable models.

641   More studies are needed for optimal design and operation of pipeline systems and other equipment in

642   novel applications such as microchannels for cooling in microelectronics, as well as many traditional

643   cases in oil and gas, refrigeration, heat exchange, and other process industries.

655   **Appendix A**

656   **Error estimation for the current friction factor calculations**

657   Error analysis of the calculated variables is important to provide an estimation of uncertainty

658   propagation due to measurements. Here, the quantity of interest is the interfacial friction factor. To

659   estimate it, we substitute Equation (14) in Equation (5), which yields a relationship for calculating the

660   interfacial friction factor in terms of all the measured experimental quantities of the pressure gradient,

661   liquid film thickness, and core density (a function of the measured liquid film velocity):

$$f_i = \frac{\frac{D - 2t}{4}\left(-\frac{dP}{dz} - \rho_c g\right)}{\frac{1}{2}\rho_c u_c^2} \tag{A1}$$

662   The quantities in Equation (A1) that are dominant in the uncertainty determination are $-\frac{dP}{dz}$, ρ_c, t, u_c,

663   and u_{lf}. The uncertainty in f_i is caused by the random errors in the measurements and can be given as

664   a relative error. Thus,

$$\frac{\delta f_i}{f_i} = \sqrt{\frac{(\delta S)^2 + (\delta \rho_c)^2}{(S + \rho_c g)^2} + \left(\frac{\delta t}{D - 2t}\right)^2 + \left(\frac{\delta \rho_c}{\rho_c}\right)^2 + \left(\frac{2\delta u_c}{u_c^2}\right)^2} \tag{A2}$$

665   where $S = -\frac{dP}{dz}$, and δ represents the uncertainties in the respective quantities. For pressure gradient

666   measurements, the uncertainty in $-\frac{dP}{dz}$ is $\pm(\sqrt{(0.04)^2 + (0.04)^2}) = \pm0.057\%$ based on the

667   manufacturer quoted error of ±0.04% for each transducer. These give 0.42–1.58 Pa/m uncertainty in

668   pressure gradient for the current experiments (See Table 3 for the actual values of pressure gradient

669   obtained). The specified range of measurement of the transducers is (0–1.5 barg ±0.04%). For film

670   thickness (measurements were between 0.7–1.3 mm), the uncertainty is ±3.3% as estimated by three

671   repeated film measurements; while for the film velocity, it is $\delta u_{lf} = \pm 8\%$ of local measurements (see

672   Aliyu et al. [40]). The uncertainty in the gas core density is not readily available since they are

673   derived quantities. Therefore, the uncertainties in ρ_c and u_c are deduced from their definitions in

674   Equations (6) and (7), respectively

675   The uncertainty in ρ_c in Equation (A2) is deduced from the definition of ρ_c in Equation (7). The

676   wetted area A_{lf} of liquid film and the input liquid mass flow rate in Equations (8) and (13) are

677   substituted in Equation (7) and simplified. This yields an expression for ρ_c in terms of u_{lf}:

$$\rho_c = \rho_l - \frac{\varepsilon(\rho_l - \rho_g)}{\varepsilon + \left(1 - \frac{\rho_l u_{lf} A_{lf}}{\dot{m}_l}\right)\frac{\varepsilon}{(1-\varepsilon)}\frac{1-x}{x}\frac{\rho_g}{\rho_l}} \tag{A3}$$

678   where $\dot{m}_l$ is the liquid input mass flow rate (in kg/s). Now,

$$\delta(\rho_c) = \delta(u_{lf})\frac{\partial \rho_c}{\partial u_{lf}} \tag{A4}$$

679   where $\frac{\partial \rho_c}{\partial u_{lf}}$ is obtained by differentiating Equation (A3). After rearranging,

$$\frac{\partial \rho_c}{\partial u_{lf}} = \frac{\varepsilon(\rho_l - \rho_g)\dfrac{\varepsilon}{1-\varepsilon}\dfrac{1-x}{x}\dfrac{\rho_g}{\rho_l}\dfrac{\rho_l A_{lf}}{\dot{m}_l}}{\left[\varepsilon + \left(1 - \dfrac{\rho_l A_{lf}}{\dot{m}_l}\right)\dfrac{\varepsilon}{1-\varepsilon}\dfrac{1-x}{x}\dfrac{\rho_g}{\rho_l}\right]^2} \tag{A5}$$

680   For the uncertainty in the core flow velocity u_c, its definition in Equation (6) is used to deduce $\delta(u_c)$:

$$\delta(u_c) = \sqrt{\left[\delta(e)\frac{\partial u_c}{\partial e}\right]^2 + \left[\delta(t)\frac{\partial u_c}{\partial t}\right]^2} \tag{A6}$$

681   where $\frac{\partial u_c}{\partial e}$ and $\frac{\partial u_c}{\partial t}$ are obtained by differentiating Equation (6) with respect to e and t respectively.

682   Thus,

$$\frac{\partial u_c}{\partial e} = \frac{u_{sl}}{(D - 2t)^2} \tag{A7}$$

683   and

$$\frac{\partial u_c}{\partial t} = \frac{4t(u_{sg} + u_{sl}e)}{(D - 2t)^3} \tag{A8}$$

684 where the entrained droplet fraction e is determined experimentally from the measured liquid film

685 velocity using Equation (1). Lastly, the percentage error in f_i for each experimental condition is

686 calculated as follows:

$$Err(f_i) = \frac{\delta f_i}{f_i} \times 100\% \tag{A9}$$

687 As similarly shown in our previous publication [40], the errors for determining the interfacial friction

688 factor from the experimental measurements using Equations (A1)–(A9) are between 5 and 15%, with

689 a majority of errors in the vicinity of 7–13% (Figure A 1).

690

691 **Figure A 1: Experimental uncertainties in f_i**

692

693 **References**

694 [1] R. J. Belt, J. M. C. Van't Westende, and L. M. Portela, "Prediction of the interfacial shear-
695   stress in vertical annular flow," *Int. J. Multiph. Flow*, vol. 35, no. 7, pp. 689–697, 2009.

696 [2] G. B. Wallis, *One Dimensional Two-Phase Flow*, vol. null. New York: McGraw-Hill, 1969.

697 [3] E. O. Moeck, "Annular-dispersed two-phase flow and critical heat flux," p. 206, 1970.

698 [4] W. H. Henstock and T. J. Hanratty, "The interfacial drag and the height of the wall layer in
699   annular flows," *AIChE J.*, vol. 22, no. 6, pp. 990–1000, 1976.

700 [5] J. C. Asali, T. J. Hanratty, and P. Andreussi, "Interfacial Drag and Film Height for Vertical
701   Annular Flow," *Am. Inst. Chem. Eng.*, vol. 31, no. 6, pp. 895–902, 1985.

702 [6] L. . Fore, S. . Beus, and R. . Bauer, "Interfacial friction in gas–liquid annular flow: analogies to
703   full and transition roughness," *Int. J. Multiph. Flow*, vol. 26, no. 11, pp. 1755–1769, Nov.
704   2000.

705 [7] R. V. A. Oliemans, B. F. M. F. M. Pots, and N. Trompé, "Modelling of annular dispersed two-
706   phase flow in vertical pipes," *Int. J. Multiph. Flow*, vol. 12, no. 5, pp. 711–732, Sep. 1986.

707 [8] I. Kataoka and M. Ishii, "Drift flux model for large diameter pipe and new correlation for pool
708   void fraction," *Int. J. Heat Mass Transf.*, vol. 30, no. 9, pp. 1927–1939, Sep. 1987.

709 [9] N. K. Omebere-Iyari, "The effect of pipe diameter and pressure in vertical two-phase flow,"

31

710   University of Nottingham, 2006.

711   [10] N. K. Omebere-iyari, B. J. Azzopardi, D. Lucas, M. Beyer, and H. Prasser, "The
712   characteristics of gas / liquid flow in large risers at high pressures," vol. 34, pp. 461–476, 2008.

713   [11] R. Kaji and B. J. Azzopardi, "The effect of pipe diameter on the structure of gas / liquid flow
714   in vertical pipes," *Int. J. Multiph. Flow*, vol. 36, no. 4, pp. 303–313, 2010.

715   [12] D. J. Peng, M. Ahmad, C. P. Hale, O. K. Matar, and G. F. Hewitt, "Flow regime transitions in
716   large diameter pipes," in *7th International Conference on Multiphase Flow*, 2010, pp. 1–9.

717   [13] L. Lao, L. Xing, and H. Yeung, "Behaviours of elongated bubbles in a large diameter riser,"
718   no. 1998, pp. 381–392, 2012.

719   [14] J. P. Schlegel, S. Miwa, S. Chen, T. Hibiki, and M. Ishii, "Experimental study of two-phase
720   flow structure in large diameter pipes," *Exp. Therm. Fluid Sci.*, vol. 41, no. 2012, pp. 12–22,
721   Sep. 2012.

722   [15] T. R. Smith, J. P. Schlegel, T. Hibiki, and M. Ishii, "Two-phase flow structure in large
723   diameter pipes," *Int. J. Heat Fluid Flow*, vol. 33, no. 1, pp. 156–167, Feb. 2012.

724   [16] B. J. Azzopardi, S. Taylor, and D. B. Gibbons, "Annular two phase flow in a large diameter
725   tube," Harwell, Oxfordshire, UK, 1982.

726   [17] G. P. Van der Meulen, "Churn-Annular Gas-Liquid Flows in Large Diameter Vertical Pipes,"
727   University of Nottingham, 2012.

728   [18] R. M. Nedderman and C. J. Shearer, "The motion and frequency of large disturbance waves in
729   annular two-phase flow of air-water mixtures," *Chem. Eng. Sci.*, vol. 18, no. 10, pp. 661–670,
730   Oct. 1963.

731   [19] Y. Zhao, C. N. Markides, O. K. Matar, and G. F. Hewitt, "Disturbance wave development in
732   two-phase gas-liquid upwards vertical annular flow," *Int. J. Multiph. Flow*, vol. 55, pp. 111–
733   129, 2013.

734   [20] N. K. Omebere-Iyari and B. J. Azzopardi, "A Study of Flow Patterns for Gas/Liquid Flow in
735   Small Diameter Tubes," *Chem. Eng. Res. Des.*, vol. 85, no. 2, pp. 180–192, 2007.

736   [21] J. F. Klausner, B. T. Chao, and S. L. Soo, "An Improved Correlation for Two-Phase Frictional
737   Pressure Drop in Boiling and Adiabatic Downflow in the Annular Flow Regime," *Proc. Inst.*
738   *Mech. Eng. Part C J. Mech. Eng. Sci.*, vol. 205, no. 5, pp. 317–328, Sep. 1991.

739 [22] A. Cioncolini, J. R. Thome, and C. Lombardi, "Unified macro-to-microscale method to predict
740 two-phase frictional pressure drops of annular flows," *Int. J. Multiph. Flow*, vol. 35, no. 12, pp.
741 1138–1148, 2009.

742 [23] T. Fukano and T. Furukawa, "Prediction of the effects of liquid viscosity on interfacial shear
743 stress and frictional pressure drop in vertical upward gas–liquid annular flow," *Int. J. Multiph.*
744 *Flow*, vol. 24, no. 4, pp. 587–603, Jun. 1998.

745 [24] K. Hori, M. Nakasamomi, K. Nishikawa, and K. Sekoguchi, "Study of ripple region in annular
746 two-phase flow (Third report, effect of liquid viscosity on gas-liquid interfacial character and
747 friction factor)," *Trans. Jap. Soc. Mech. Eng.*, vol. 44, no. 387, pp. 3847–3856, 1978.

748 [25] T. Fukano, A. Ito, K. Miyabe, and Y. Takamatsu, "Liquid films flowing concurrently with air
749 in horizontal duct. (6th report Generation of disturbance waves and its relation with the
750 breakdown of liquid film)," *Transactions of the Japan Society of Mechanical Engineers Series*
751 *B*, vol. 51, no. 462. pp. 503–512, 1985.

752 [26] W. Ambrosini, P. Andreussi, and B. J. Azzopardi, "A physically based correlation for drop
753 size in annular flow," *Int. J. Multiph. Flow*, vol. 17, no. 4, pp. 497–507, Jul. 1991.

754 [27] T. Fukano, Y. Kawakami, A. Qusaka, and A. Tominaga, "Interfacial shear stress and holdup in
755 an air - water Annular two-phase flow," in *Proceedings of the ASME-JSME Thermal*
756 *Engineering Joint Conference: Reno, Nevada, March 17-22, 1991*, 1991, vol. 2, p. 217.

757 [28] A. J. Holt, B. J. Azzopardi, and M. W. Biddulph, "Calculation of Two-Phase Pressure Drop for
758 Vertical Upflow in Narrow Passages by Means of a Flow Pattern Specific Model," *Chem. Eng.*
759 *Res. Des.*, vol. 77, no. 1, pp. 7–15, 1999.

760 [29] S. Wongwises and W. Kongkiatwanitch, "Interfacial friction factor in vertical upward gas-
761 liquid annular two-phase flow," *Int. Commun. Heat Mass Transf.*, vol. 28, no. 3, pp. 323–336,
762 2001.

763 [30] M. H. S. Zangana, "Film behaviour of vertical gas-Liquid Flow in a large diameter pipe," no.
764 May, p. 222, 2011.

765 [31] A. Skopich, E. Pereyra, C. Sarica, and M. Kelkar, "Pipe-diameter effect on liquid loading in
766 vertical gas wells," *SPE Prod. Oper.*, vol. 30, no. 2, pp. 164–176, 2015.

767 [32] D. G. Owen, "An experimental and theoretical analysis of equilibrium annular flows,"
768 University of Birmingham, 1986.

769   [33]   C. J. Shearer and R. M. Nedderman, "Pressure gradient and liquid film thickness in co-current
770   upwards flow of gas/liquid mixtures: Application to film-cooler design," *Chem. Eng. Sci.*, vol.
771   20, no. 7, pp. 671–683, Jul. 1965.

772   [34]   P. Alia, L. Cravarolo, A. Hassid, and E. Pedrocchi, "Phase and Velocity Distribution in Two-
773   phase Adiabatic Annular Dispersed Flow," Milan, Italy, 1968.

774   [35]   L. B. Fore and A. E. Dukler, "Droplet deposition and momentum transfer in annular flow,"
775   *AIChE J.*, vol. 41, no. 9, pp. 2040–2046, Sep. 1995.

776   [36]   L. B. Fore and A. E. Dukler, "Droplet deposition and momentum transfer in annular flow,"
777   *AIChE J.*, vol. 41, no. 9, pp. 2040–2046, 1995.

778   [37]   A. A. Almabrok, "Gas-Liquid two-phase flow in up and down vertical pipes," Cranfield
779   University, 2014.

780   [38]   A. M. Aliyu, "Vertical annular gas-liquid two-phase flow in large diameter pipes," Cranfield
781   University, 2015.

782   [39]   A. A. Almabrok, A. M. Aliyu, L. Lao, and H. Yeung, "Gas/liquid flow behaviours in a
783   downward section of large diameter vertical serpentine pipes," *Int. J. Multiph. Flow*, vol. 78,
784   pp. 25–43, 2016.

785   [40]   A. M. Aliyu, L. Lao, A. A. Almabrok, and H. Yeung, "Interfacial shear in adiabatic downward
786   gas/liquid co-current annular flow in pipes," *Exp. Therm. Fluid Sci.*, vol. 72, pp. 75–87, 2016.

787   [41]   M. W. E. Coney, "The theory and application of conductance probes for the measurement of
788   liquid film thickness in two-phase flow," *J. Phys. E.*, vol. 6, no. 9, pp. 903–911, Sep. 1973.

789   [42]   J. E. Koskie, I. Mudawar, and W. G. Tiederman, "Parallel-wire probes for measurement of
790   thick liquid films," *Int. J. Multiph. Flow*, vol. 15, no. 4, pp. 521–530, 1989.

791   [43]   N. A. Tsochatzidis, T. D. Karapantsios, M. V. Kostoglou, and A. J. Karabelas, "A conductance
792   probe for measuring liquid fraction in pipes and packed beds," *Int. J. Multiph. Flow*, vol. 18,
793   no. 5, pp. 653–667, 1992.

794   [44]   B.-A. Lee, B.-J. Yun, K.-Y. Kim, and S. Kim, "Estimation of local liquid film thickness in
795   two-phase annular flow," *Nucl. Eng. Technol.*, vol. 44, no. 1, pp. 71–78, Feb. 2012.

796   [45]   H.-M. Prasser, M. Beyer, H. Carl, S. Gregor, D. Lucas, H. Pietruske, P. Schütz, and F.-P.
797   Weiss, "Evolution of the structure of a gas–liquid two-phase flow in a large vertical pipe,"
798   *Nucl. Eng. Des.*, vol. 237, no. 15–17, pp. 1848–1861, Sep. 2007.

799   [46]   M. J. Da Silva, S. Thiele, L. Abdulkareem, B. J. Azzopardi, and U. Hampel, "High-resolution
800   gas–oil two-phase flow visualization with a capacitance wire-mesh sensor," *Flow Meas.*
801   *Instrum.*, vol. 21, no. 3, pp. 191–197, Sep. 2010.

802   [47]   M. J. Da Silva, E. Schleicher, and U. Hampel, "Capacitance wire-mesh sensor for fast
803   measurement of phase fraction distributions," *Meas. Sci. Technol. Meas. Sci. Technol*, vol. 18,
804   no. 18, pp. 2245–2251, 2007.

805   [48]   M. J. Da Silva, S. Thiele, L. Abdulkareem, B. J. Azzopardi, and U. Hampel, "High-resolution
806   gas – oil two-phase flow visualization with a capacitance wire-mesh sensor," *Flow Meas.*
807   *Instrum.*, vol. 21, no. 3, pp. 191–197, 2010.

808   [49]   N. Hall Taylor, G. F. Hewitt, and P. M. C. Lacey, "The motion and frequency of large
809   disturbance waves in annular two-phase flow of air-water mixtures," *Chem. Eng. Sci.*, vol. 18,
810   pp. 537–552, 1963.

811   [50]   P. Sawant, M. Ishii, T. Hazuku, T. Takamasa, and M. Mori, "Properties of disturbance waves
812   in vertical annular two-phase flow," *Nucl. Eng. Des.*, vol. 238, no. 12, pp. 3528–3541, 2008.

813   [51]   G. F. Hewitt and N. Hall Taylor, *Annular Two-phase Flow*. Oxford: Pergamon Press, 1970.

814   [52]   K. W. McQuillan and P. B. Whalley, "Flow patterns in vertical two-phase flow," *Int. J.*
815   *Multiph. Flow*, vol. 11, no. 2, pp. 161–175, 1985.

816   [53]   G. F. Hewitt, "Co-Current and Counter-Current Two Phase Annular Flow," *9th Australasian*
817   *Fluid Mechanics COnference*. pp. 19–28, 1986.

818   [54]   Q. Al-Yarubi, "Phase flow measurements of annular flows," University of Huddersfield, 2010.

819   [55]   R. E. Vieira, M. Parsi, C. F. Torres, B. S. McLaury, S. A. Shirazi, E. Schleicher, and U.
820   Hampel, "Experimental characterization of vertical gas-liquid pipe flow for annular and liquid
821   loading conditions using dual Wire-Mesh Sensor," *Exp. Therm. Fluid Sci.*, vol. 64, pp. 81–93,
822   2015.

823   [56]   A. Cioncolini and J. R. Thome, "Entrained liquid fraction prediction in adiabatic and
824   evaporating annular two-phase flow," *Nucl. Eng. Des.*, vol. 243, pp. 200–213, 2012.

825   [57]   M. Ishii and K. Mishima, "Droplet entrainment correlation in annular two-phase flow," *Int J*
826   *Heat Mass Transf.*, vol. 32, no. 10, pp. 1835–1846, Oct. 1989.

827   [58]   P. Sawant, M. Ishii, and M. Mori, "Prediction of amount of entrained droplets in vertical
828   annular two-phase flow," *Int. J. Heat Fluid Flow*, vol. 30, no. 4, pp. 715–728, 2009.

829 [59] Y. Taitel, D. Bornea, and A. E. Dukler, "Modelling flow pattern transitions for steady upward
830   gas-liquid flow in vertical tubes," *AIChE J.*, vol. 26, no. 3, pp. 345–354, May 1980.

831 [60] G. F. Hewitt and D. N. Roberts, "Studies of Two Phase Patterns by Simultaneous X-Ray and
832   Flash Photography," Harwell, Berkshire, 1969.

833 [61] C. J. Shearer and R. M. Nedderman, "Pressure gradient and liquid film thickness in concurrent
834   upwards flow of gas/liquid mixtures: application to film cooler design," *Chem. Eng. Sci.*, vol.
835   20, no. 671, pp. 671–683, 1965.

836 [62] Shell, "Gas / Liquid Separators - Type Selection and Design Rules Manual," 2007.

837 [63] B. J. Azzopardi, "Mechanisms of entrainment in annular two phase flow.PDF," Harwel,
838   Oxfordshire, UK, 1983.

839 [64] S. Jayanti, A. Tokarz, and G. F. Hewitt, "Theoretical investigation of the diameter effect on
840   flooding in countercurrent flow," *Int. J. Multiph. Flow*, vol. 22, no. 2, pp. 307–324, Apr. 1996.

841 [65] G. B. Wallis, "The onset of droplet entrainment in annular gas-liquid flow," General Electric
842   Co. General Engineering Lab., Schenectady, NY, RPRT, 1962.

843 [66] J. R. Barbosa, G. F. Hewitt, G. König, and S. M. Richardson, "Liquid entrainment, droplet
844   concentration and pressure gradient at the onset of annular flow in a vertical pipe," *Int. J.*
845   *Multiph. Flow*, vol. 28, no. 6, pp. 943–961, 2002.

846 [67] A. Cioncolini, J. R. Thome, and C. Lombardi, "Algebraic turbulence modeling in adiabatic
847   gas-liquid annular two-phase flow," *Int. J. Multiph. Flow*, vol. 35, no. 6, pp. 580–596, 2009.

848 [68] M. Narcy, "flow boiling in straight heated tube under normal and microgravity conditions,"
849   University of Toulouse, 2015.

850

Figures:
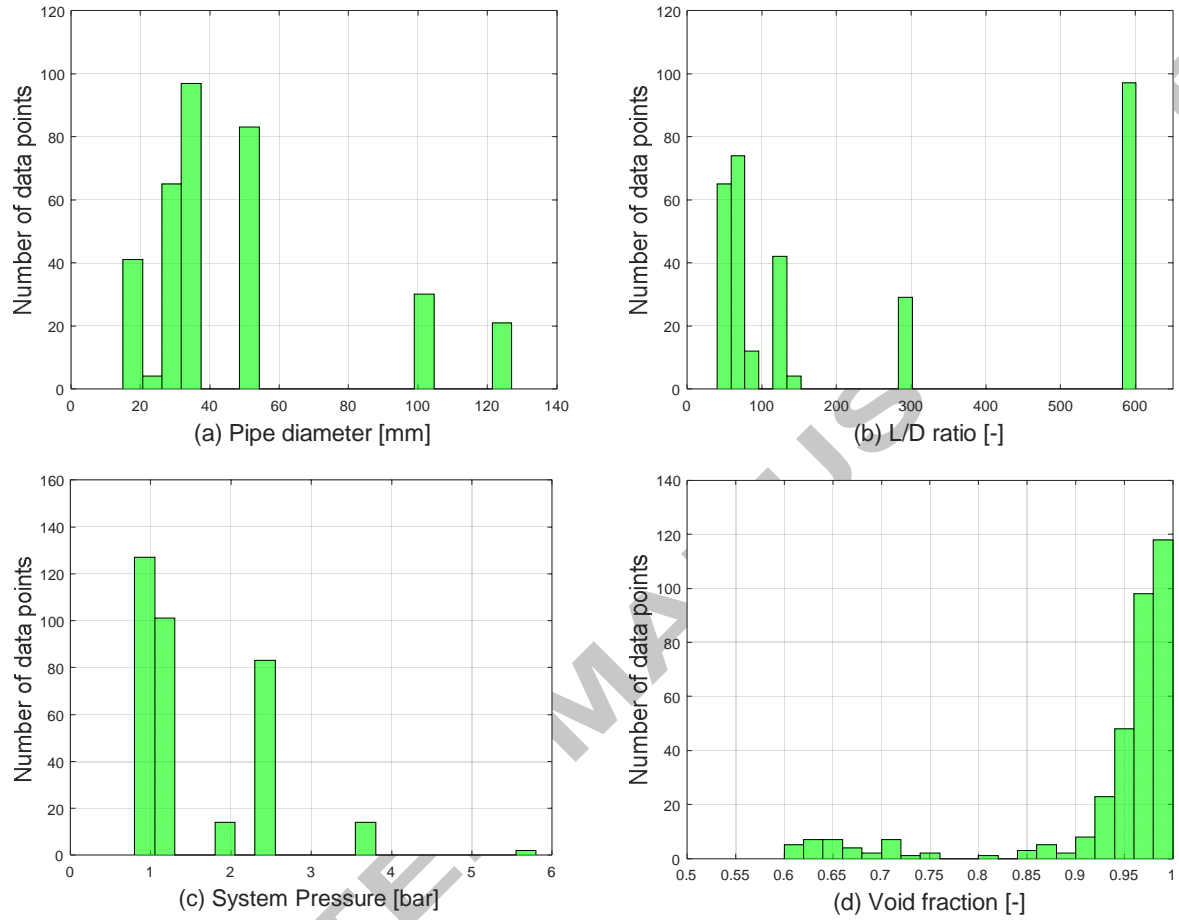
Figure 1: Histograms showing selected parameters of the experimental database given in Error! Reference source not found.
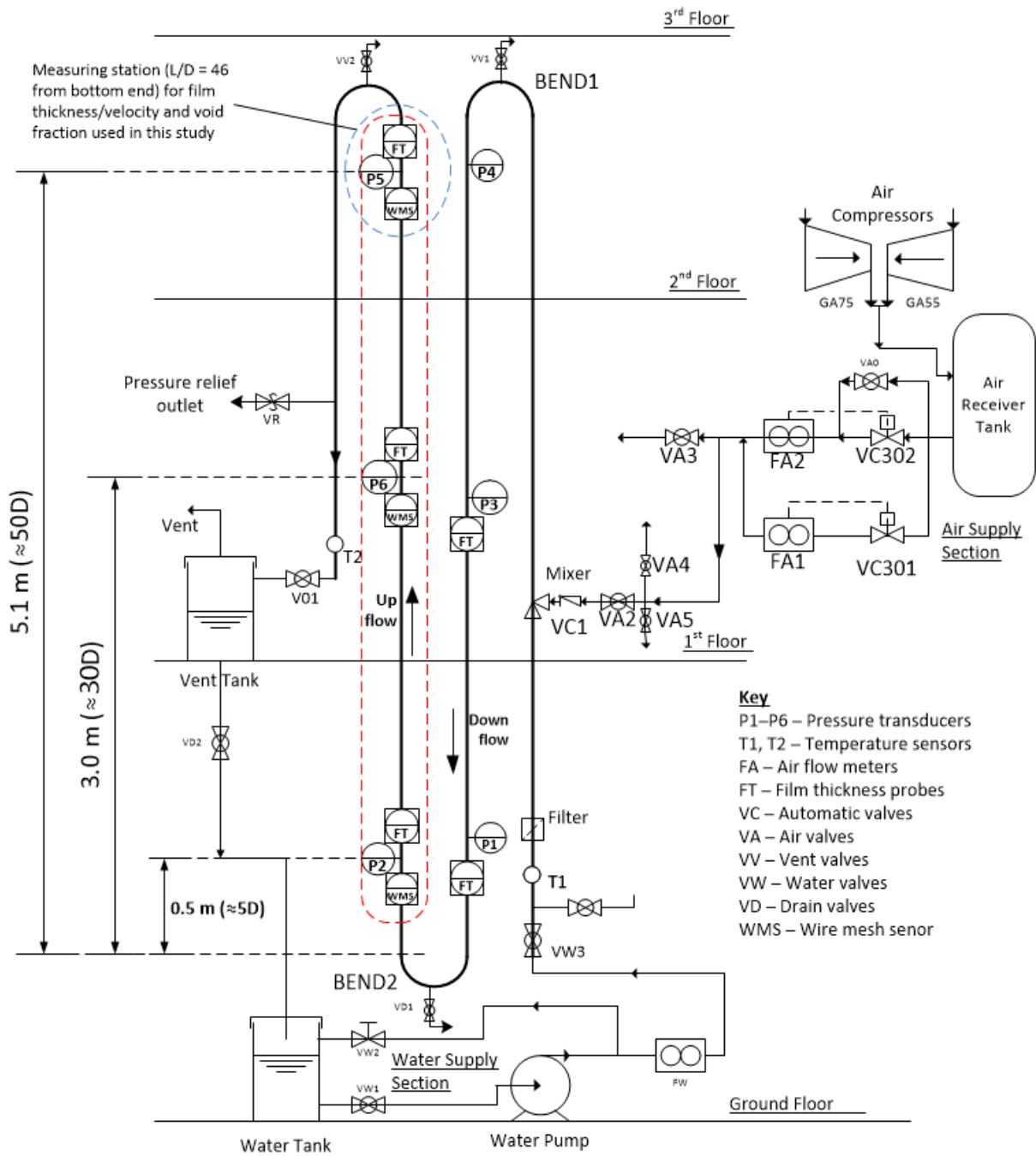
Figure 2: Serpent Rig facility indicating the upward section used for this study
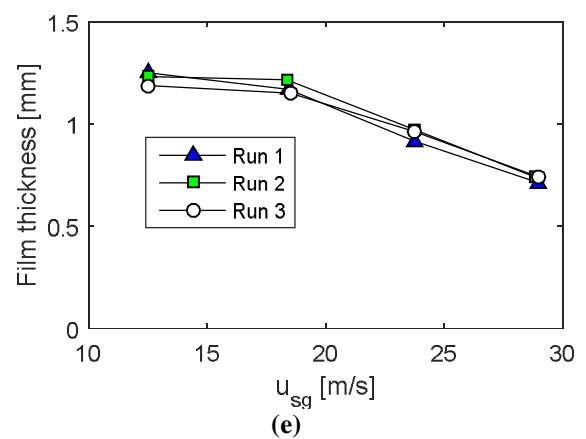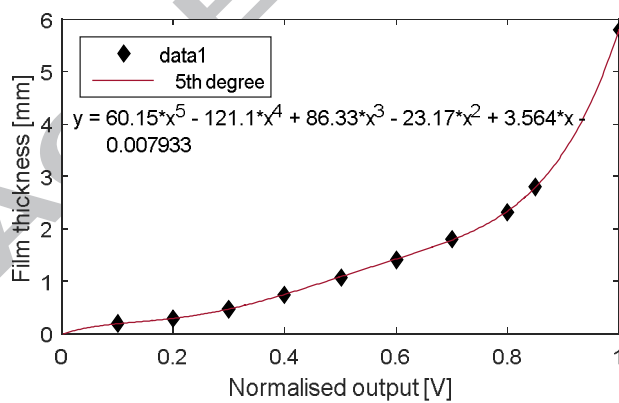
(a)

(b)

(c)

(d)

(e)

Figure 3: (a) film thickness sensor spool with four flush-mounted probes (b) details of individual sensor design (all dimensions in mm) (c)) blocks of different diameters used for probe calibration (d) sample of film thickness calibration curve (e) Repeatability tests for film thickness probes showing the mean film thickness at u_{sl} = 0.1 m/s. For more conditions, see Almabrok [37]
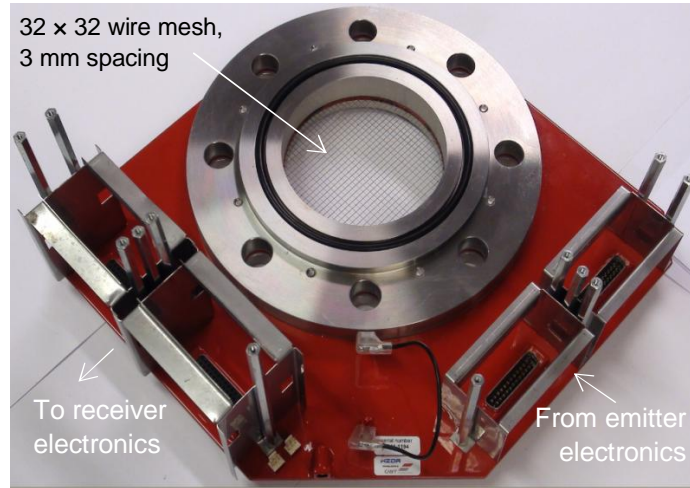
Figure 4: Capacitance wire mesh sensor used in this study
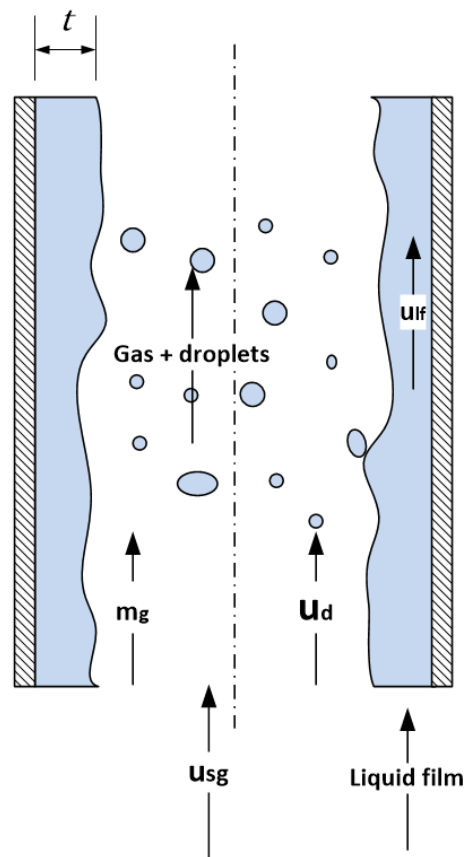
Figure 5: Representation of annular flow with droplets
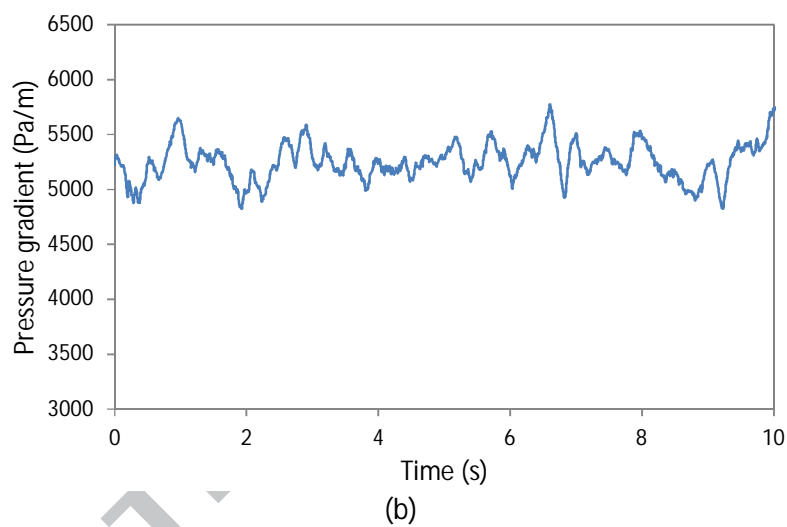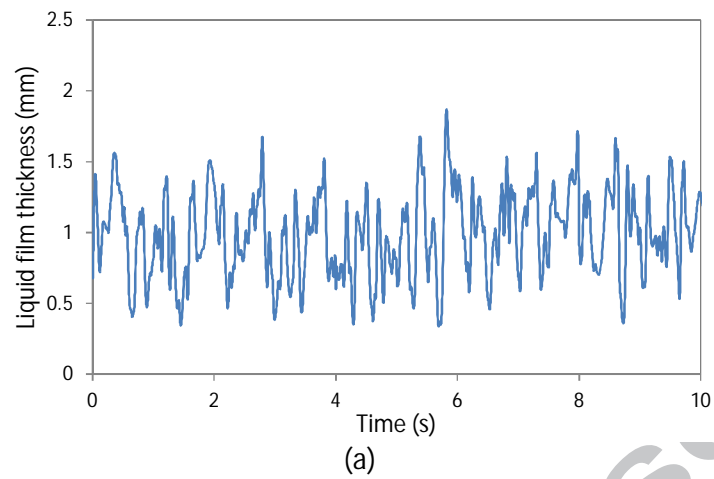
Figure 6: Examples of time series data for (a) liquid film thickness and (b) pressure gradient with a superficial liquid velocity of 1.0 m/s and superficial gas velocity of 18.56 m/s
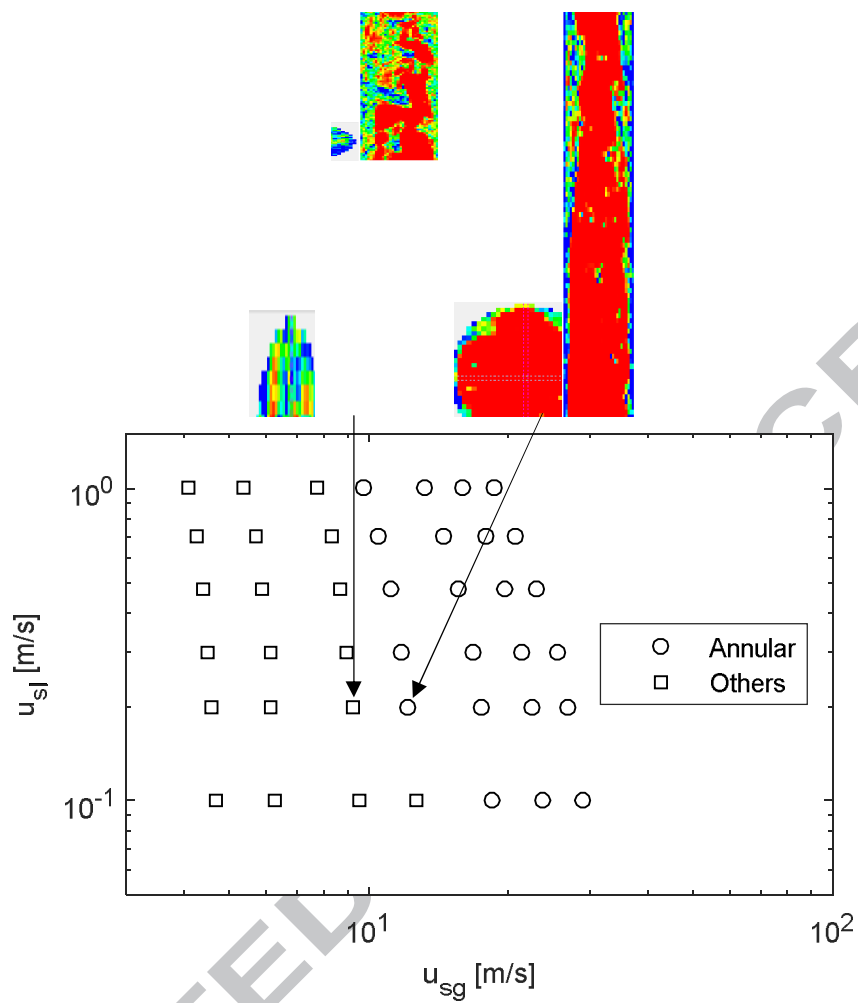
Figure 7: Effect of fluid superficial velocities on flow regime map produced by visual observations aided by WMS visualisation
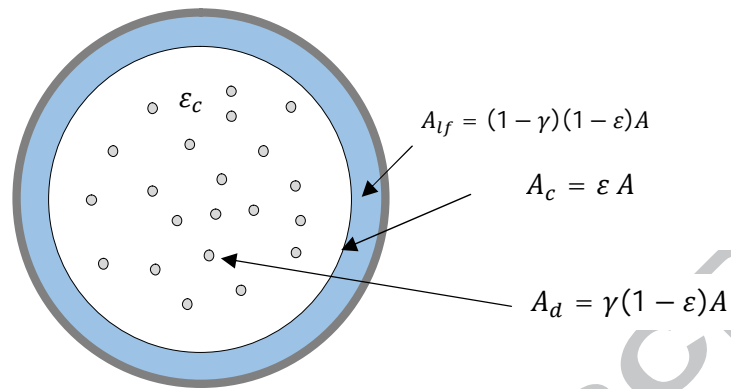
Figure 8: Representation and notation of the various phases (film, gas, and droplets) occupying the total pipe area. Subscript *d* denotes droplets. Where γ, ε, and ε_c are the droplet holdup, void fraction and core void fraction respectively (Cioncolini et al. [22])
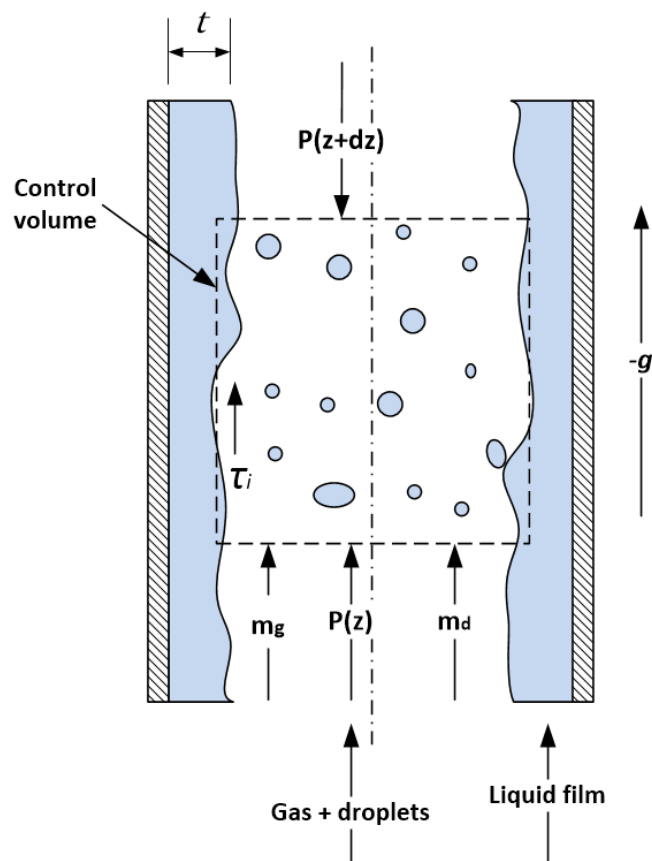
Figure 9: Control volume for the momentum balance in Equation Error! Reference source not found.**.**
Based on the schematic by Wongwises and Kongkiatwanitch [29]
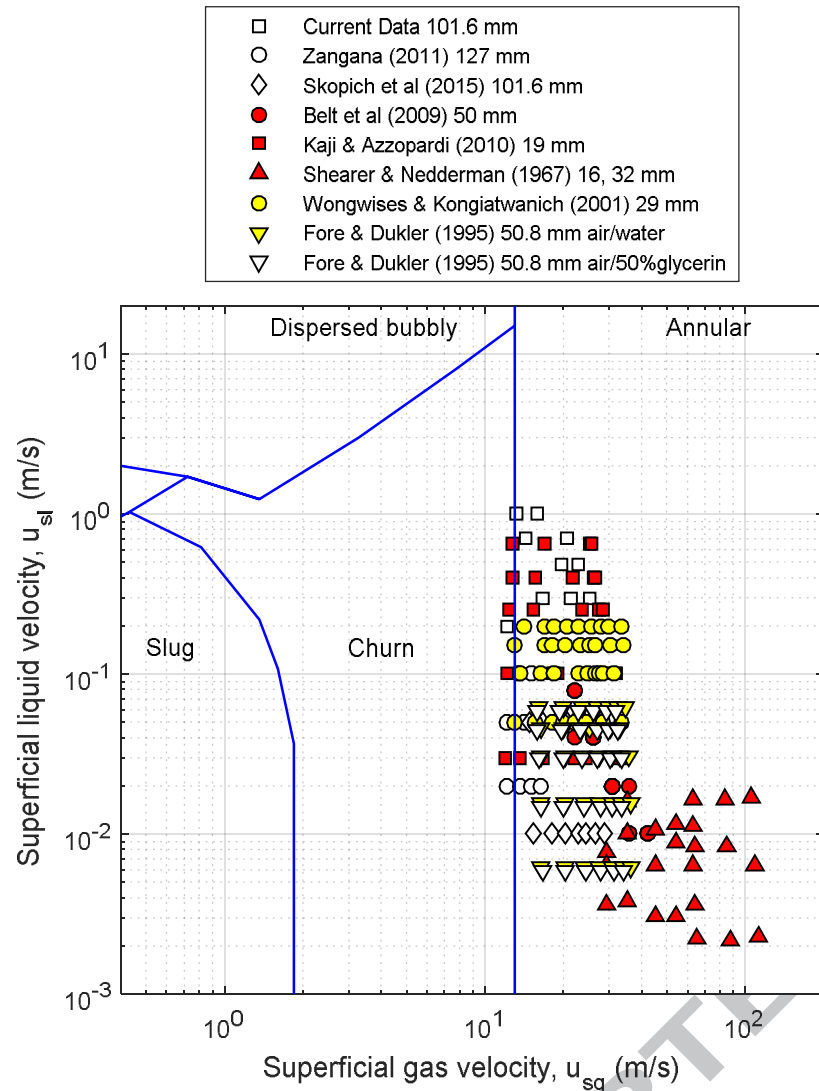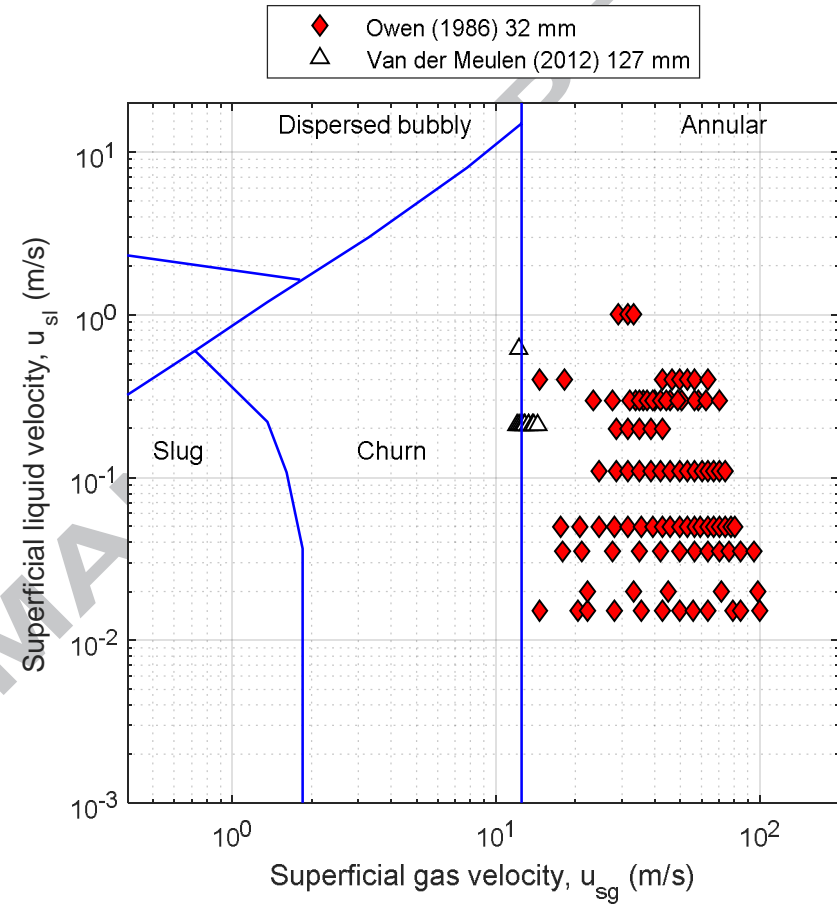
Figure 10: Experimental data against the Taitel et al. [59] **flow regime map**
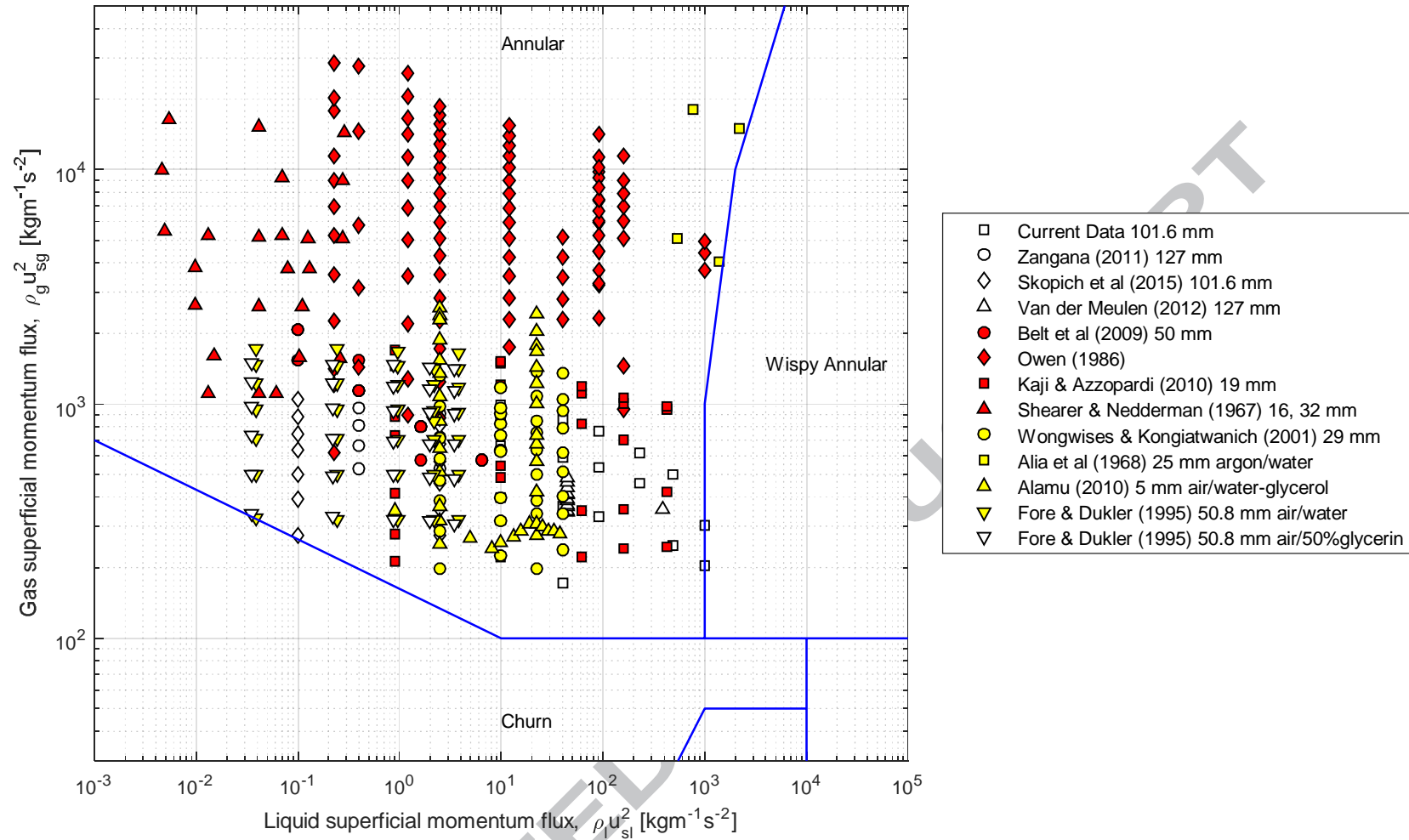
Figure 11: Experimental data bank against Hewitt and Roberts [60] **flow regime map showing all data are in the annular flow regime**
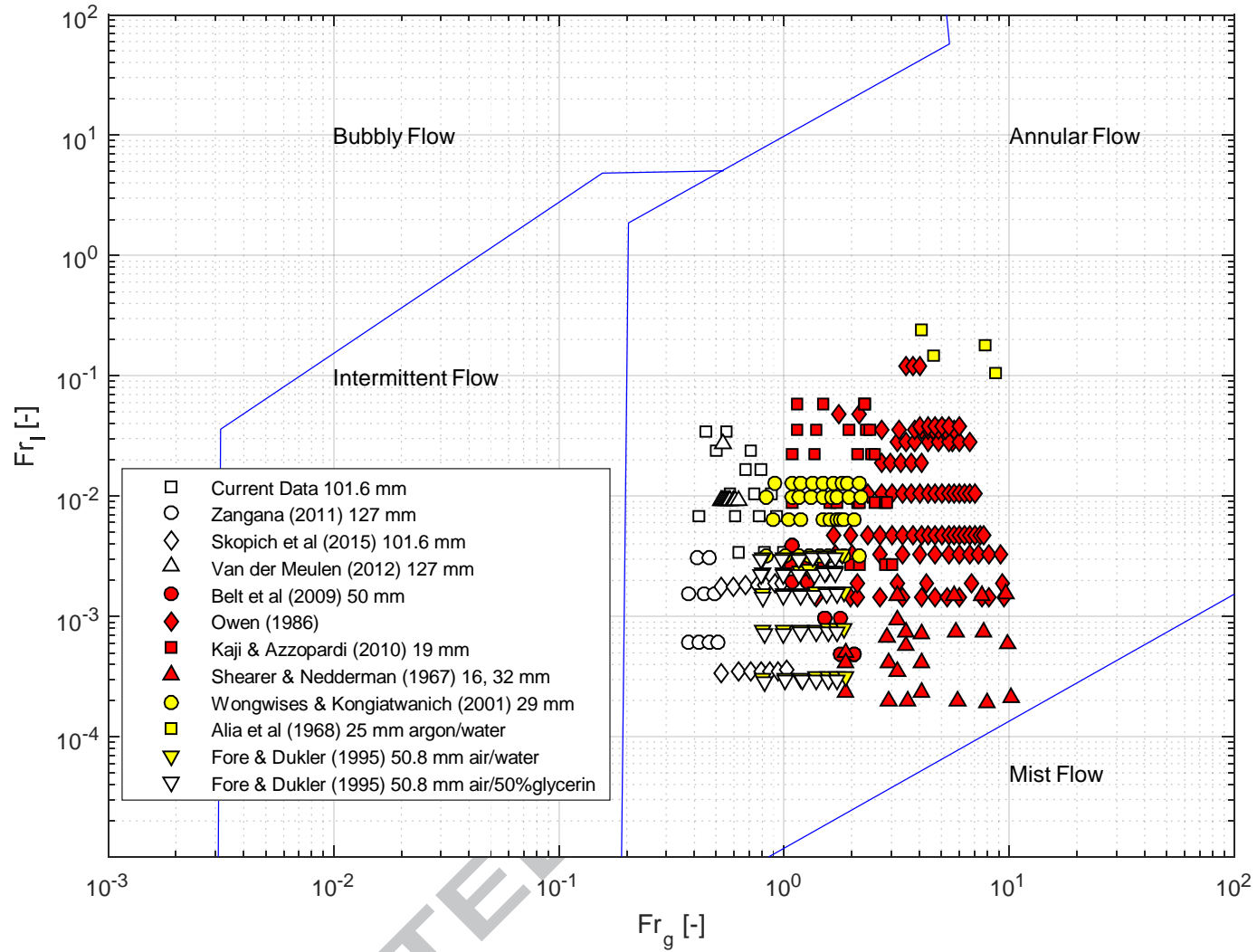
Figure 12: experimental databank against the Shell [62] **flow regime map**
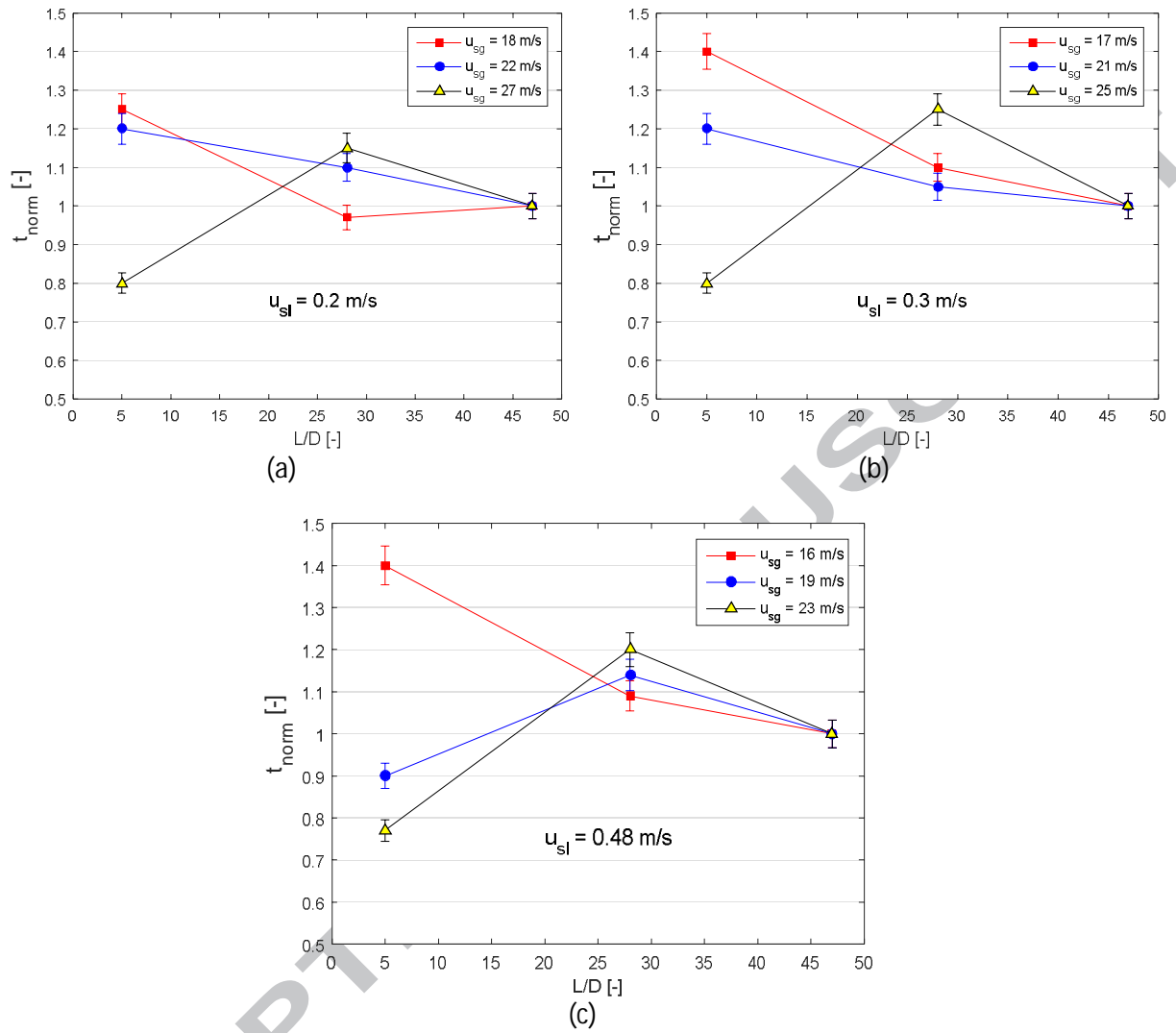
Figure 13: Normalised liquid film thickness axial development in the upwards flowing section of the rig

(See Almabrok [37] for more)
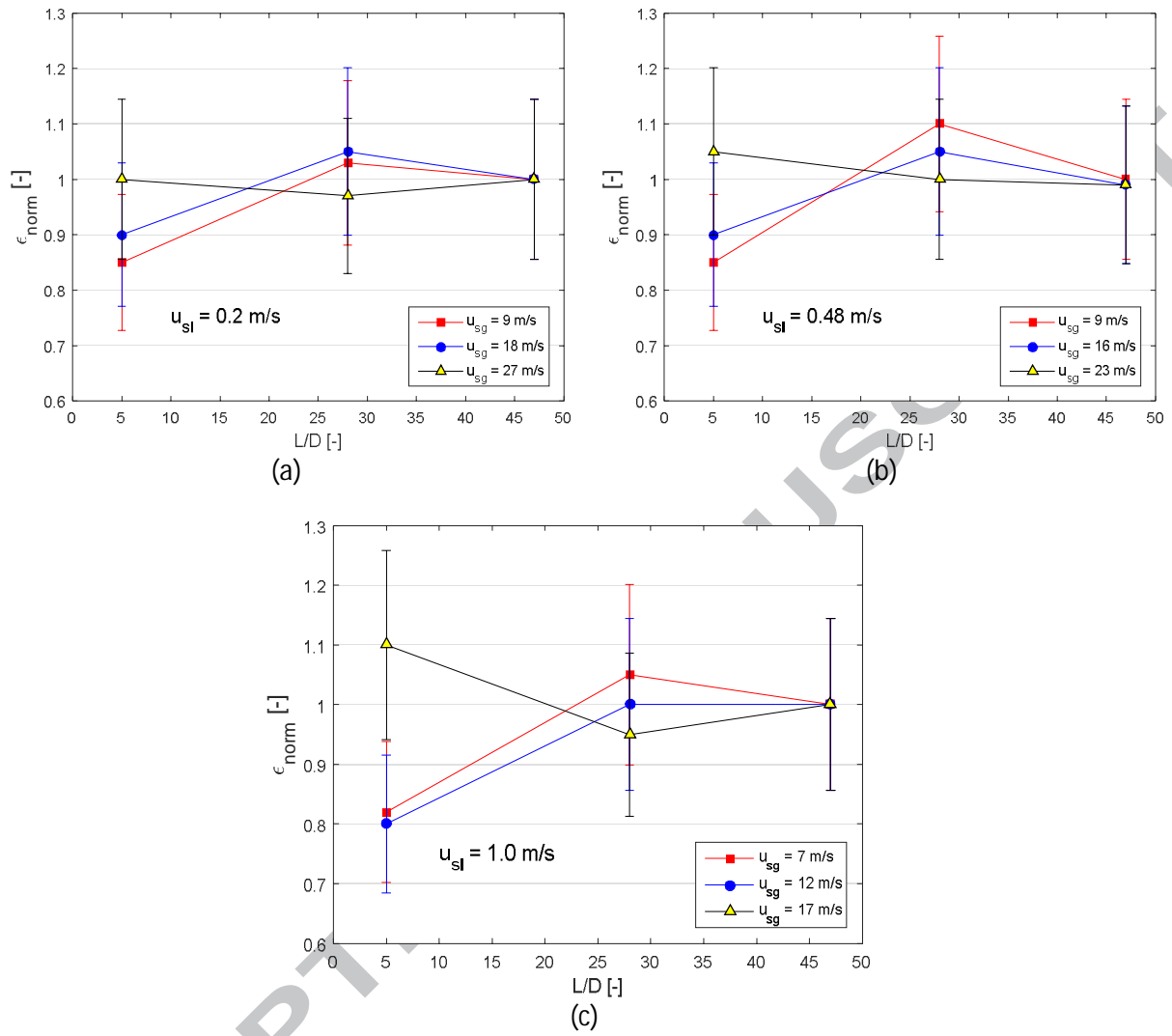
Figure 14: Normalised gas void fraction axial development in the upwards flowing section of the rig
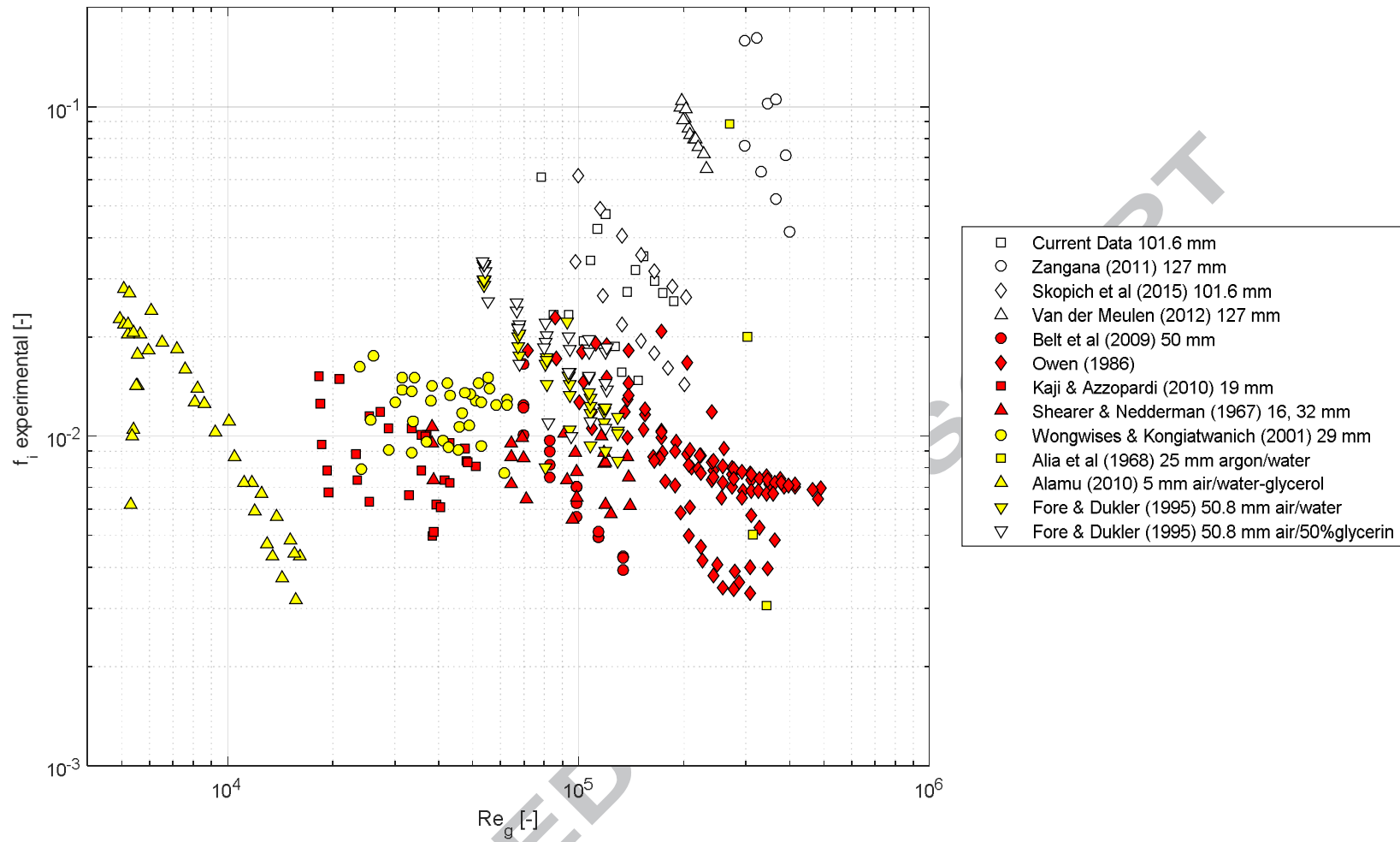
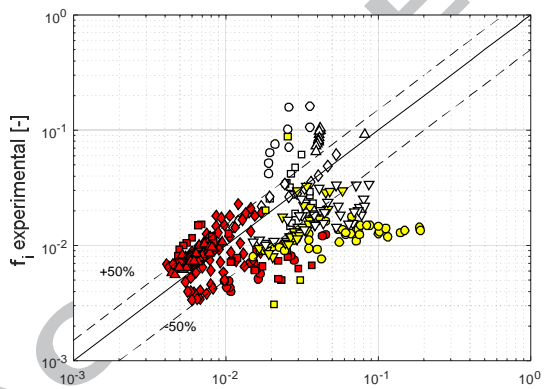**Figure 15: Experimental interfacial friction factors versus superficial gas Reynolds number**
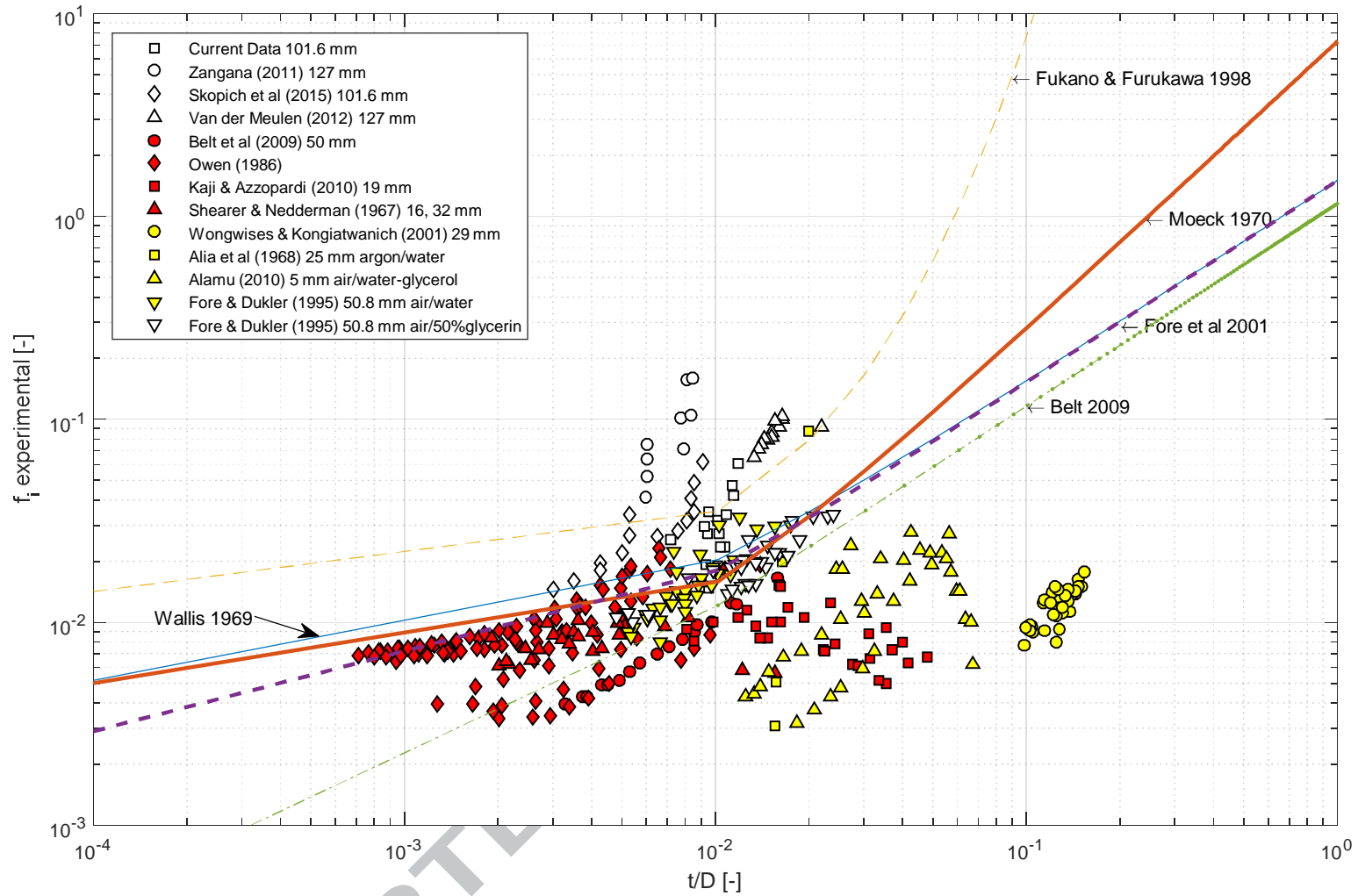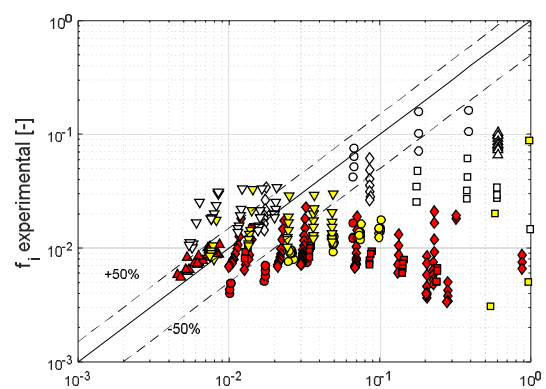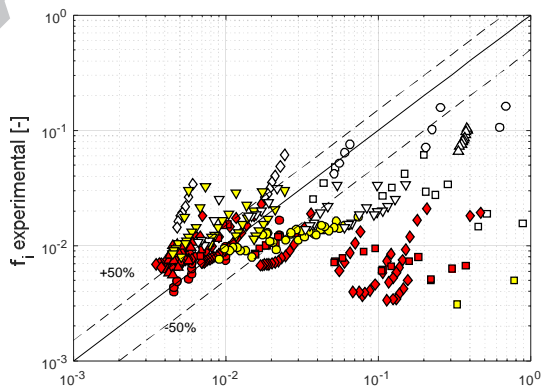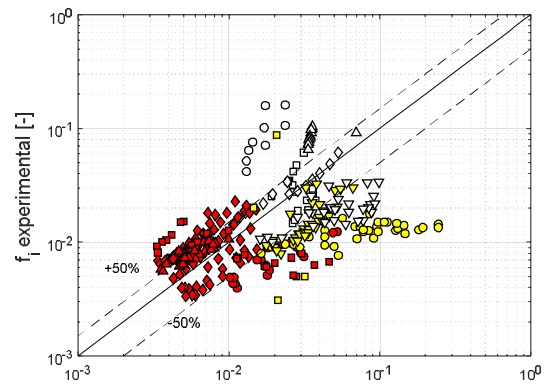
Figure 16: Comparison of current and other experimental friction factors with Wallis-type correlations
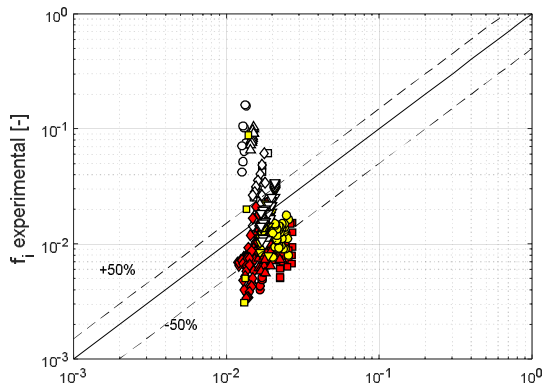
(a) f_i calculated (Blasius 1913) [-]
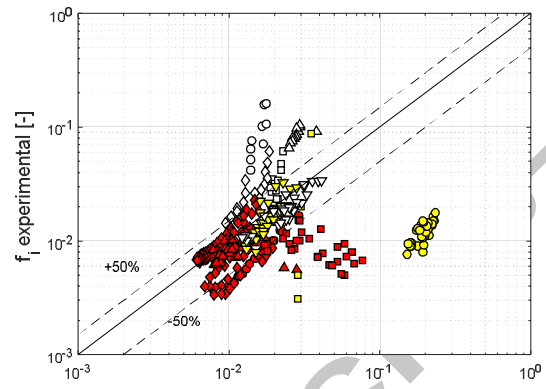
(b) f_i calculated (Wallis 1969) [-]
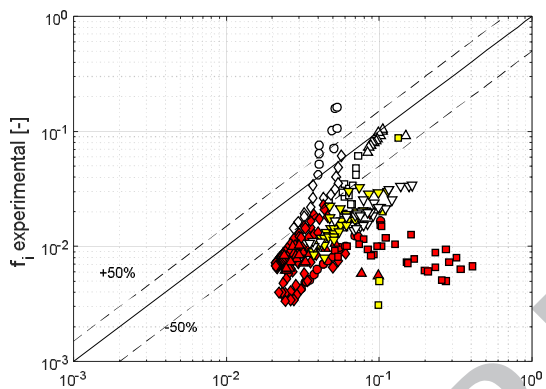
(c) f_i calculated (Moeck 1970) [-]
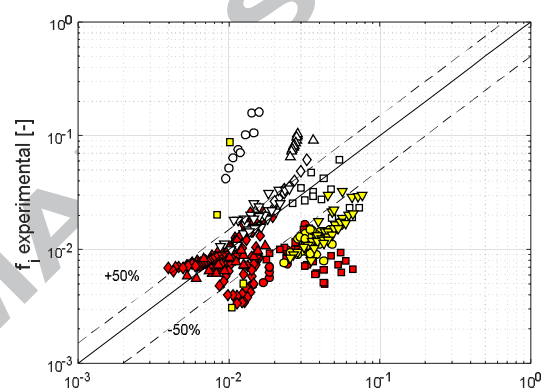
(d) f_i calculated (Hori 1976) [-]

(e) f_i calculated (Asali et al 1985) [-]

(f) f_i calculated (Fukano et al 1985) [-]

(g) f_i calculated (Fukano et al 1991) [-]

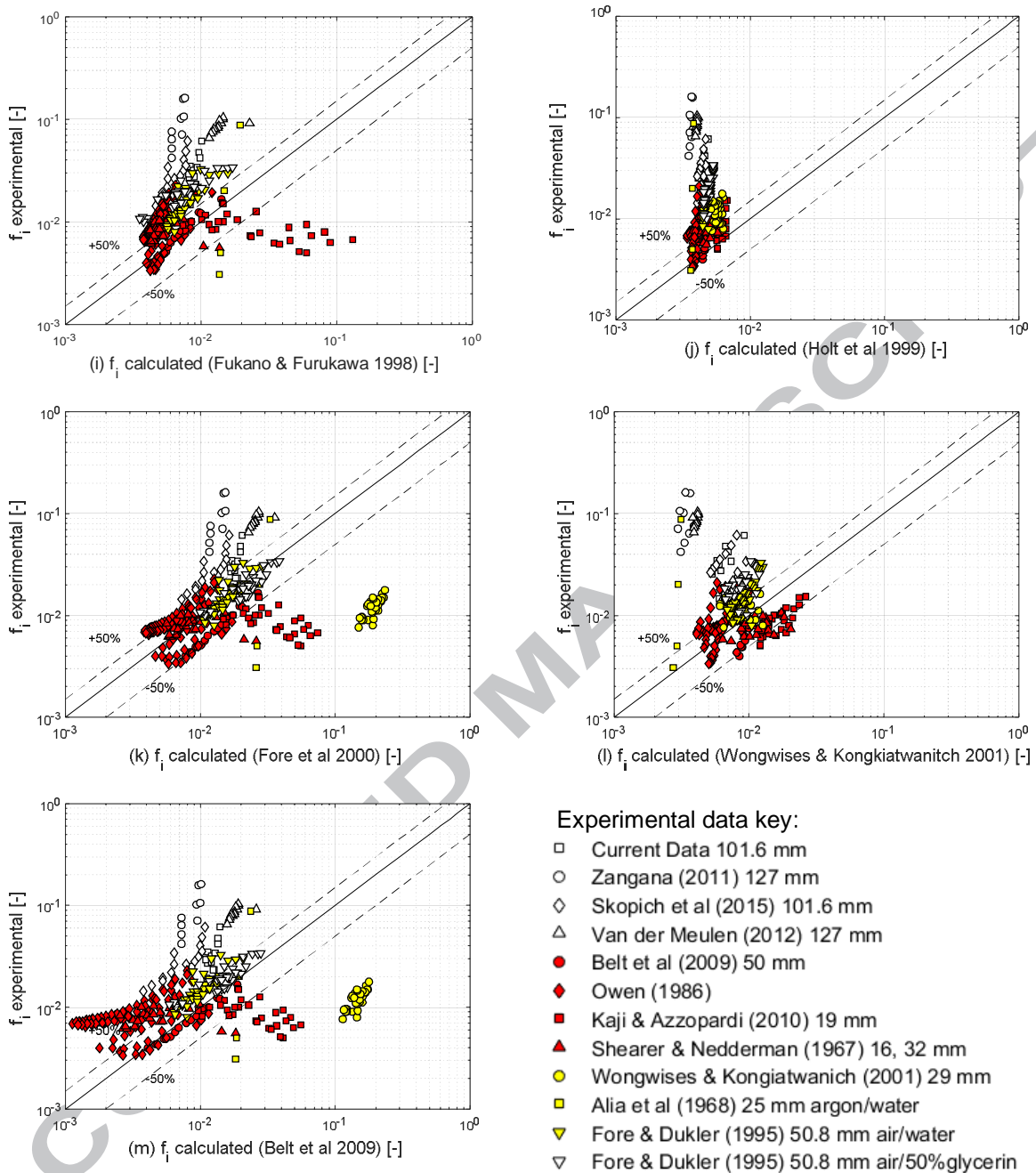(h) f_i calculated (Ambrosini et al 1991) [-]

Figure 17: Comparison of 332 interfacial friction factor data points with predictions of various correlations
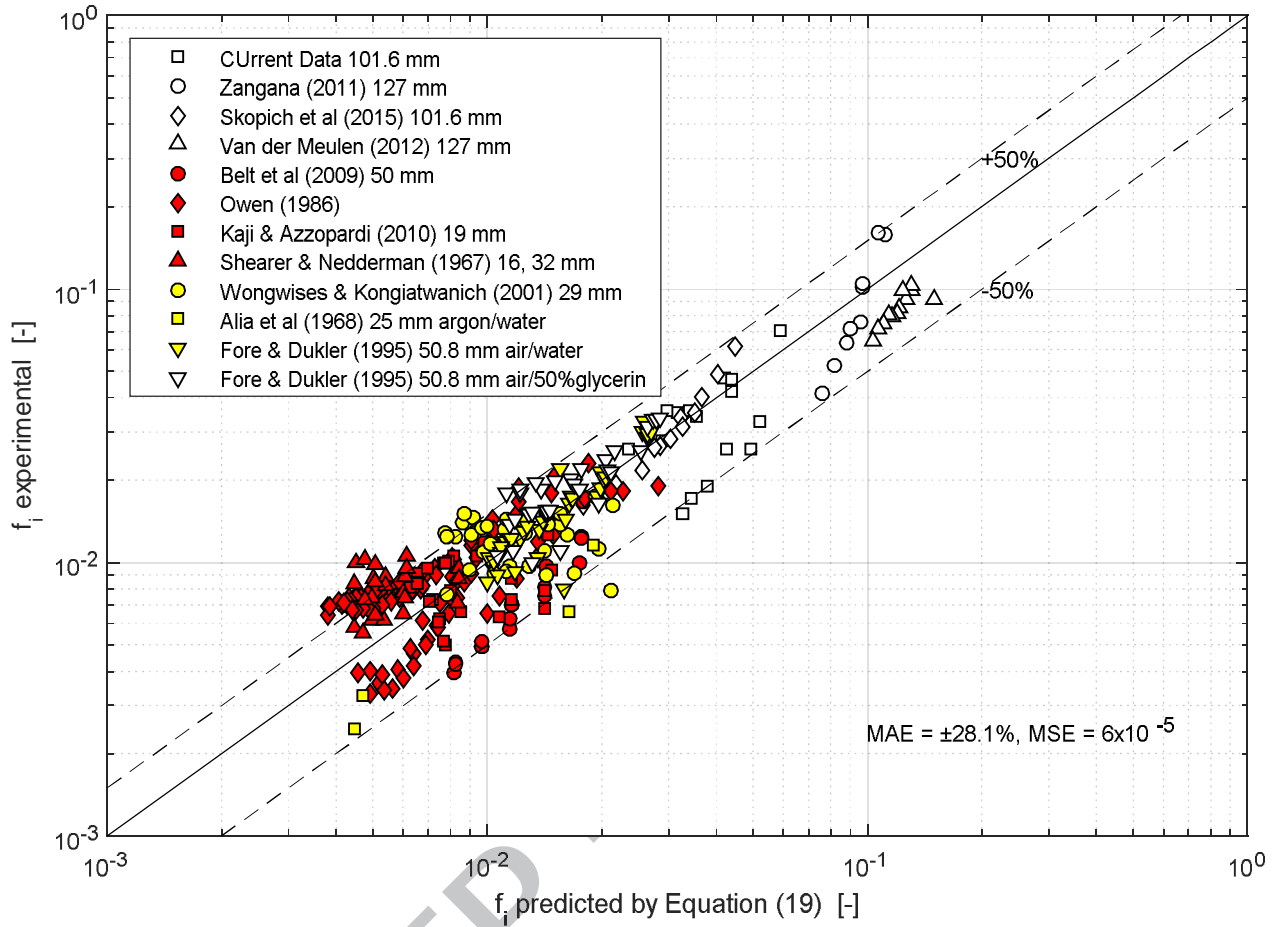
Figure 18: Predictions of proposed correlation compared with entire experimental database
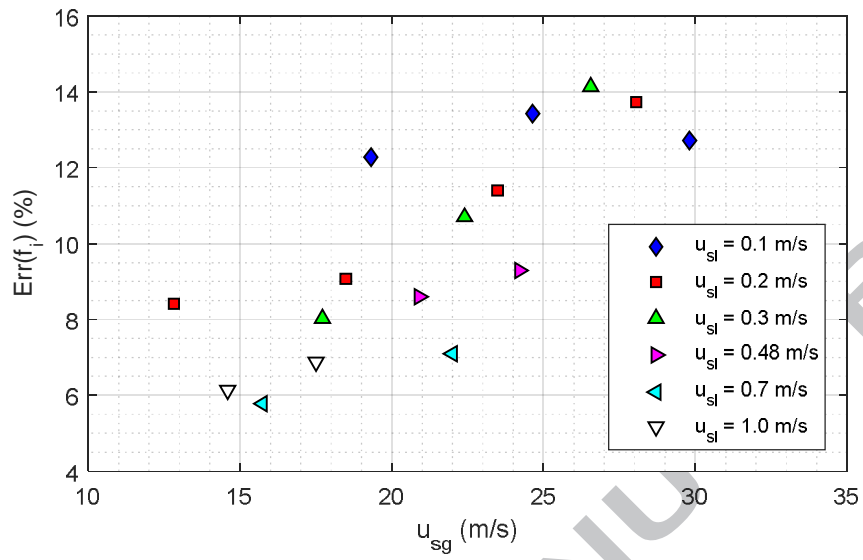
Figure A1: Experimental uncertainties in f_i

Tables

Table 1: Reported interfacial friction factor correlations used for comparison with the current experimental data

Author(s)	Equation	Remarks
Blasius	$f_i = 0.316\, Re_g^{-0.25}$	Valid for Re up to 10^5
Wallis [2]	$f_i = 0.005[1 + 300t/D]$	Theoretical model
Moeck [3]	$f_i = 0.005[1 + 1458(t/D)^{1.42}]$	Pipe 24 mm, steam/water
Hori et al. [24]	$f_i = 1.13\, Re_g^{-0.89} Re_l^{0.68} Fr_g^{0.25} Fr_l^{-0.45}(\mu_l/\mu_w)^{0.7}$, $Fr_g = u_{sg}/\sqrt{gD}$, $Re_g = \rho_g u_{sg} D/\mu_g$	Pipe 13, 19.8, 26 mm, $u_{sg} = 53$–56 m/s, $u_{sl} = 0.006$–0.0061 m/s
Asali et al. [5]	$f_i = f_g[1 + Re_g^{-0.2}(Re_g\sqrt{f_i/2}\; t/D - 4)]$, where $f_g = 0.316\, Re_g^{-0.25}$	Pipe 22.9, 42 mm, air/water, air/glycerine, 1–2 bar system pressure
Fukano et al. [25]	$f_i = f_g[1 + 1 \times 10^{-5} Re_g^{0.7} Re_l^{0.65} X^{0.52}]$, $X = \sqrt{\frac{\Delta P_{lo}}{\Delta L}/\frac{\Delta P_{go}}{\Delta L}}$, $\Delta P_{LO}/\Delta L = \frac{1}{2}(f_L/D)\rho_L u_{sl}^2$, $\Delta P_{gO}/\Delta L = \frac{1}{2}(f_g/D)\rho_g u_{sg}^2$	Rectangular duct, 80×10 mm, air/water, 0.98–1 bar pressure, $Re_l = 10$–300, $u_{sg} = 10$–50 m/s
Ambrosini et al. [26]	$f_i = f_g[1 + 13.8 We^{0.2} Re_g^{-0.6}(t^+ - 200\sqrt{\rho_g/\rho_l})]$, for $\dot{m} > 100\, kgm^{-2}s^{-1}$, where $t_g^+ = 0.19 Re_{lf}^{0.7}$	Pipe 10–42.2 mm, air/water, helium/water, air/various hydrocarbons, 0.2 – 1.9 bar
Fukano et al. [27]	$f_i = f_g[1 + 8.53 \times 10^{-4} X^{2.82} Re_g^2/Re_l]$	Pipe, 10, 16, 26 mm, 1.02 – 1.35 bar, $u_{sg} = 20 – 60$ m/s, $u_{sl} = 0.06 – 0.1$ m/s
Fukano and Furukawa [23]	$f_i = 0.425(12 + \nu_l/\nu_w)^{-1.33}(1 + 12t/D)^8$	Pipe 4.6 mm, air/water, air/glycerol, 1–1.2 bar, $u_{sg} = 10$–50 m/s, $u_{sl} = 0.04$–0.3 m/s
Holt et al. [28]	$f_i = f_g[1 + 13.8 We^{0.175} Re_g^{-0.7}]$, for $\dot{m} > 100\, kgm^{-2}s^{-1}$	Pipe 5, 10 mm, square duct 7.7×2.6 mm, trapezoidal duct, 2×7×4.4 mm, air/water, nitrogen/water, helium/water, air/glycerol, 0.2–1.5 bar pressure
Fore et al. [6]	$f_i = 0.005[1 + 300(t/D - 0.0015)]$	Rectangular duct, 101.6×5.08 mm, nitrogen/water, 3.4–17 bar
Wongwises and Kongkiatwanitch [29]	$f_i = 17.172\, Re_g^{-0.768}(t/D)^{-0.253}$	Pipe 29 mm, air/water, 1 bar pressure
Belt et al. [1]	$f_i = 1.158 t/D + 3.143 \times 10^{-4}$	Pipe 19 mm, air/water, 1 bar pressure

Table 2: Experimental data for upward interfacial friction factor (all air/water except stated otherwise)

S/No.	Authors	D [mm]	L/D [-]	Test pressure [bara]	u_{sl} range [m/s]	u_{sg} range [m/s]	Measurements made	Number of data points	Symbol
1	Current	101.6	46	1.0–1.4	0.1-1.0	10–29	dP/dz, t, u_{lf}	23	□
2	Zangana [30]	127	66	1.0	0.02–1.00	10–17	dP/dz, ε, τ_w	9	⊙
3	Skopich et al. [31]	101.6	58–92	0.9–1.2	0.01–0.05	14–27	dP/dz, ε	14	◇
4	Van der Meulen [17]	127	87	2.0	0.02–0.70	10–17	dP/dz, ε	12	△
5	Belt et al. [1]	50	120, 140	1.0	0.01–0.08	22–42	dP/dz, t	18	•
6	Owen [32]	32	600	2.0–4.0	0.02–1.00	14–100	dP/dz, e	97	♦
7	Kaji and Azzopardi [11]	19	300	1.2	0.03–0.65	10–34	dP/dz, ε	29	▪
8	Shearer and Nedderman [33]	16, 32	133–267	1.1	0.02–0.10	10–16	dP/dz, t	24	▲
9	Wongwises and Kongkiatwanitch [29]	29	41	1.0	0.05–0.2	9–34	dP/dz, t	35	○
10	Alia et al. [34]*	25	140	2–6	0.07–1.5	7–150	dP/dz, t	6	□
11	Fore and Dukler [35]	50.8	69	1.0	0.006–0.06	16–36	dP/dz, t, e, τ_w	35	▽
12	Fore and Dukler [35]**	50.8	69	1.0	0.006–0.06	16–36	dP/dz, t, e, τ_w	30	▽
	Total							332	

*Argon–Water, ** Air–50%glycerin, fluid combination

Table 3: Averaged measured quantities for the air–water system in the upward section of the Serpent Rig

Test Pressure (bara)	u_{sl} (m/s)	u_{sg} (m/s)	t (mm)	u_{lf} (m/s)	dP/dz (Pa/m)
1.09	0.10	18.39	1.2	0.86	1039.2
1.13	0.10	23.66	1.0	1.00	1268.6
1.15	0.10	28.87	0.7	1.01	1592.2
1.10	0.20	12.08	1.2	0.78	1680.4
1.14	0.20	17.51	1.2	0.80	1419.6
1.18	0.20	22.41	1.0	1.02	1488.2
1.23	0.20	26.90	1.0	2.02	1576.5
1.13	0.30	11.70	1.3	0.74	1878.4
1.18	0.30	16.74	1.1	0.73	2505.9
1.23	0.30	21.33	1.0	1.03	2172.5
1.29	0.30	25.47	0.9	2.03	1890.2
1.17	0.48	11.16	1.2	0.98	1794.1
1.25	0.48	15.63	1.1	1.08	1839.2
1.32	0.48	19.62	1.0	1.10	2045.1
1.40	0.48	22.87	1.0	1.14	2441.2
1.23	0.70	10.50	1.1	0.89	3068.6
1.33	0.70	14.45	1.1	1.10	2452.9
1.42	0.70	17.91	1.0	1.12	2149.0
1.53	0.70	20.59	0.9	1.19	2145.1
1.32	1.00	9.65	1.2	0.94	2284.3
1.44	1.00	13.15	1.1	1.30	2772.5
1.56	1.00	15.98	1.0	1.37	3260.8
1.67	1.00	18.56	0.9	1.42	3937.3

Table 4: Statistical comparison between predictions of proposed and previous correlations

Correlation \ Statistic	MSE*	MAE**	Percentage of points within ±50% error band
Proposed	0.00006	28.1	83.85
Blasius	0.00051	123.3	28.57
Wallis [2]	0.00412	259.7	49.69
Moeck [3]	0.27280	1814.1	6.83
Hori et al. [24]	0.00067	139.5	43.48
Asali et al. [5]	0.00099	115.2	49.38
Ambrosini et al. [26]	0.00157	143.0	44.72
Fukano et al. [27]	0.06933	678.6	46.89
Fukano & Furukawa [23]	5.59788	5468.3	45.03
Holt et al. [28]	0.00066	139.5	36.34
Fore et al. [6]	0.00404	231.6	57.76
Wongwises & Kongkiatwanich [29]	0.00062	49.6	54.97
Belt et al. [1]	0.00250	185.3	41.93

*MSE is the Mean Square Error defined as $\frac{1}{n}\sum_{i}^{n}\left(f_{i,exp}-f_{i,pred}\right)^2$

**MAE is the percentage Mean Absolute Error defined as $\frac{1}{n}\sum_{i}^{n}\left|\frac{f_{i,exp}-f_{i,pred}}{f_{i,exp}}\right| \times 100$

Highlights

- Gas–liquid two-phase flow experiments conducted in a large diameter flow loop
- Data were collected for interfacial friction factor in upwards annular flow regimes
- Data were also gathered from other sources spanning both small and large diameter pipes
- Previous correlations' predictions deviated at high shear regions mainly for large pipes
- Improved correlation is proposed to fit the diverse database of more than 300 data points

Interfacial friction in upward annular gas–liquid two-phase flow in pipes

Aliyu, A. M.